Nitrogen Doped Zinc Oxide Thin Film

by

Sonny Xiao-zhe Li

B. S. (University of California, Berkeley) 2000

A thesis submitted in partial satisfaction of the

requirements for the degree of

Master of Science

in

Engineering – Material Science and Engineering

in the

GRADUATE DIVISION

of the

UNIVERSITY of CALIFORNIA, BERKELEY

Committee in Charge:

Prof. Eugene E. Haller, Chair

Prof. Oscar D. Dubón Jr.

Prof. Ture Kenneth Gustafson

Fall 2003

The thesis of Sonny Xiao-zhe Li is approved:

_____

Chair Date

_____

Date

_____

Date

University of California, Berkeley

Fall 2003

Acknowledgments

I would like to thank Professor Eugene Haller for his continuous support, advice, and encouragement, which make this experience enjoyable. In addition, I would like to thank Bill Hansen for his advice and support throughout the project. His wealth of knowledge and his vigorous ability of converting thoughts into designs and actual equipments are greatly admired. His guidance, support, and the large amount of time he spent on teaching me are greatly appreciated.

Besides, I would like to acknowledge many other people who have contributed directly and indirectly to this project. Jonathan Denlinger of the ALS performed the NEXAFS spectroscopy to our ZnO samples. His measurements are the key result of this project. Jeff Beeman gave much helpful advice and performed all the ion implantations. Dr. Junqiao Wu taught me many characterization techniques including Hall effect, PL, and optical absorption, to name a few. His invaluable advice and friendship are also appreciated. Dr. Hauyee Chang taught me how to operate an X-ray diffraction machine. Dr. Kin Man Yu helped me with RBS measurements and various other analyses. I would like to thank Professor Hans-Joachim Queisser for his scientific advice and encouragement. Professor R. Helbig of Universitat Erlangen-Nurnberg of German has provided me some of his vapor-grown ZnO single crystals.

I would like to thank all of my fellow graduate students and staff in the Haller group for their support and friendship. In particular, David Hom has helped me with various administrative details, which were very important for this project to run smoothly.

I would like to thank Professor Oscar Dubon and Professor Kenneth Gustafson for reading this thesis and providing valuable input.

This work is also supported by the director, Office of Science, Office of Basic Energy Sciences, Division of Material Sciences and Engineering, of the U. S. Department of Energy under Contract No. DE-AC03-76SF00098.

Finally, on a more personal level, I would like to thank my parents and my family for their unconditional love and support through the years. I am very grateful for what they have gone through to provide me with this opportunity of receiving an advanced education.

Index

1. Introduction

1.1 Motivation

Zinc (II) oxide (ZnO) is one of the natural chemical forms of the element zinc. Pure ZnO is colorless and crystallizes in the hexagonal (wurtzite) system. A powder form of ZnO, known as "zinc white," has been used as white pigment for over two hundred years owing to its high refractivity value and chemical stability [1]. Large amounts of ZnO are used in the rubber industry as a vulcanizing activator. In agriculture, ZnO is used as an additive to offset a lack of zinc in the soil. In cosmetics, ZnO is used in making powders, ointments, and lipsticks [2].

Wurtzite Zinc (II) Oxide is a transparent wide bandgap semiconductor with a 3.3-eV bandgap at room temperature. Poly-crystalline ZnO has been used in a wide variety of electronic applications. Ceramics made by sintering ZnO powers with a small addition of the oxides of Be, Co, Cr, Mn, or Sb have a non-linear current-voltage characteristic. Those ceramics are important materials in making varistors and other voltage limiting devices [3]. Being piezoelectric, ZnO changes shape when an electric field is applied. Polycrystalline ZnO is often sputtered to fabricate transducers [4]. Polycrystalline ZnO is also used in making phosphors [5] and transparent conducting coating on solar cells [6]. Recent advances in ZnO single crystal growth techniques have opened up new possibilities in optoelectronic device applications.

In the last few years, increasing needs for short-wavelength, high-power solid-state emitters and detectors have inspired research on wide bandgap semiconductors. Most material developments on wide bandgap semiconductors have focused on GaN (3.4

eV bandgap at room temperature) [7,8], ZnSe (2.9 eV) [9,10], and 6H-SiC (3.0 eV) [10]. Among them, GaN has gained a clear edge in optoelectronic applications since 6H-SiC is an indirect bandgap semiconductor and ZnSe forms defects under high current operation. However, recently ZnO has emerged as a possible competitor in blue and UV solid-state emitter and detector applications.

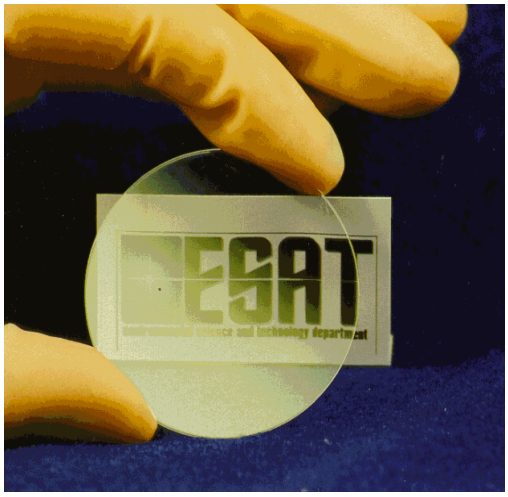

Figure 1-1: 2-inch ZnO wafer grown by Eagle-Picher Technologies [11]

ZnO applications in short-wavelength emitters and detectors might become possible because of the availability of bulk ZnO crystals. Currently 2-inch wafers, as shown in Figure 1-1, can be purchased from Eagle-Picher Technologies [11]. The ZnO wafers are grown by a seeded physical vapor transport (SPVT) process, which is a modification of conventional physical vapor transport (PVT) processes. Conventional PVT processes for II-VI compounds are typically seedless or use small seeds whereby the crystal diameter is increased during growth. The diameter enlargement process not only is slow but can also leads to high defect concentrations. The SPVT process developed by Eagle-Picher uses full-diameter seeds to grow single crystal ingots lengthwise with the growth axis along the <100> or <001> direction. Since the full diameter ingots do not require any further growth in diameter, the defect concentration is reduced, the growth rate is increased, and the processing equipment is simplified. The single crystals grown by the Eagle-Picher SPVT process have free electron concentrations of about $10^{17}/cm^3$ and mobilities of about 200 $cm^2/V{\cdot}s$ [11].

ZnO has several potential advantages over GaN in optoelectronic applications. Having a 59 meV exciton binding energy [12], ZnO is a more efficient emitter than GaN (21-25 meV exciton binding energy) at room temperature. Currently 2-inch ZnO wafers can be purchased for device fabrication or epitaxial growth but still no GaN bulk substrates are commercially available. Wet chemical processing is possible for ZnO but difficult for GaN. However, a major obstacle for ZnO in optoelectronic device applications is the production of good-quality and stable p-type material.

1.2 Asymmetry in doping

For the development of optoelectronic devices with ZnO, it is necessary to have high quality materials of both n-type and p-type. However, crystalline ZnO is naturally n-type and very difficult to dope to make p-type. There have been reports of doping ZnO intrinsically (through native defects) [13,14] and extrinsically (through impurity doping) [15] with group III elements to the point of being a metallic conductor. However, despite of a number of reports of p-type measurements in ZnO films, which will be discussed later, today there is still no reliable method of producing good quality p-type ZnO.

Despite years of investigations, the origin of this "asymmetry" in doping is still controversial. In a recent publication [16], calculations by Zhang *et al*. showed that in ZnO the zinc interstitials (Zn_i) native defect, a double donor, has a low formation enthalpy under both zinc-rich and oxygen-rich growth conditions. The native defects that can compensate Zn_i, such as oxygen interstitials (O_i) or zinc vacancies (V_{Zn}), have high formation enthalpies at zinc-rich conditions. Therefore, electrons from Zn_i are the dominant carriers for zinc-rich condition. ZnO cannot be intrinsically doped p-type via

shallow native acceptors O_i and V_{Zn} in an equilibrium process because those native acceptors can be compensated by defects such as Zn_i, oxygen vacancies (V_O), and zinc-oxygen anti-sites (Zn_O), which have low formation enthalpies under both zinc-rich and oxygen-rich conditions. Calculations from Ref. [16] also suggest that the V_O acts as an electron-hole recombination center that is responsible for the green emission at 2.4 eV commonly observed [17,18] in photoluminescence spectra of ZnO.

Van der Walle [19] suggests that hydrogen, despite being a compensator in most semiconductors, acts as a shallow donor in the ZnO lattice that causes n-type conductivity. Hydrogen is present as a carrier gas, in water vapor, and/or metal-organic chemical vapor in most crystal growth environments. It is small enough to be easily incorporated into a crystal during growth. Interstitial hydrogen is found to be amphoteric in most semiconductors. In p-type materials it donates one electron and becomes H^+, while in n-type materials it accepts one electron and becomes H^-. However, calculations from Ref. [19] show that hydrogen can be incorporated into the ZnO lattice exclusively as a donor (H^+). Early experiments [20-22] have indicated that indiffusion of hydrogen increases the conductivity of ZnO crystals. More recent experiments [23] reported 3-fold increase of electron concentration after a 14-hour exposure to deuterium plasma at 270°C. However, hydrogen in ZnO is also shown be thermally unstable. Ip *et al.* [24] implanted $2.7\times10^{19}/\mathrm{cm}^3$ hydrogen ions into ZnO single crystal. After annealing at 600°C for 5 minutes, only 0.2% of the implanted hydrogen was retained. As will be discussed later, similar annealing of our samples did not lower the electron concentration in our ZnO films, indicating that hydrogen is not a major donor source in our samples.

The difficulties of p-type doping of ZnO can be explained in part by compensation effects of native defects [25-27]. Calculations by Oba *et al.* [25] suggest that if p-type conditions exist, formation enthalpies of the compensating native donor defects are low in both the zinc-rich limit and the oxygen-rich limit. At the zinc-rich limit Zn_i, V_O, and Zn_O have low formation enthalpies while at the oxygen-rich limit Zn_i and V_O have low formation enthalpies. Those native donor defects effectively compensate p-type doping [25]. A few calculations [26,27] were done specifically for the compensation effects of nitrogen, which is the most popular p-type dopant in current research. These calculations indicate that at low nitrogen dopant levels V_O is the main compensating donor while at high nitrogen dopant levels Zn_O forms defect complexes with nitrogen acceptors, which in turn compensate the acceptor. If a plasma N_2 source is used to increase the nitrogen concentration, N acceptors are compensated by formation of N_2 substitution in oxygen sites [$(N_2)_O$] and N-acceptor – N_2 complexes. $(N_2)_O$ is a double shallow donor that is similar to $(N_2)_{Se}$ in ZnSe. The N_O–$(N_2)_O$ complex behaves as a single donor [26,27].

Other possible acceptors in ZnO, including group I elements (Li, Na, and K) and other group V elements (P and As), are less effective than nitrogen based on calculations by Park *et al*. [28]. Although substitutions by group I elements are shallow acceptors, calculations show that group I elements tend to form interstitials and actually behave as donors. P and As are deep acceptors and calculations show they can lead to formation stable AX centers, which convert acceptors into deep donors. Calculations also show that although P and As are amphoteric [28], and that they have a tendency to form P_{Zn} and As_{Zn} antisites, which are also donors.

1.3 Current state of research

Among possible dopants, nitrogen appears to be a more promising choice than other impurities since it is a known p-type dopant for ZnSe. Acceptor concentrations as high as $10^{18}/cm^3$ were obtained in ZnSe samples grown by molecular beam epitaxy (MBE) using nitrogen atom beam doping [29]. An early N-doped, p-type ZnO result was reported by Minegishi *et al*. [30]. The p-type ZnO films were grown by chemical vapor deposition (CVD) from a powder ZnO source with excess Zn onto a heated (650 – 800˚C) sapphire substrate. The N source was NH_3 carried by purified hydrogen gas, which is introduced during deposition. The resulting ZnO films have hole concentrations up to $1.5\times10^{16}/cm^3$ and show a resistivity of about 100 $\Omega\cdot$cm [30]. However, this result has not been reproduced.

One problem with N-doping is the low solubility of nitrogen in ZnO [26]. Yamamoto *et al*. [31] proposed that the solubility of nitrogen can be increased by introducing group III codopant such as Al, Ga, or In. Yamamoto *et al*.'s calculations show that reactive codopants such as Al, Ga or In could form complexes with nitrogen, which enhance the incorporation of N-acceptors and thus produce p-type ZnO [31]. Joseph *et al*. [32] reported p-type results by co-doping ZnO with Ga and N. The results of Joseph *et al.* will be discussed in detail later in this chapter.

Ryu *et al*. [33] reported p-type characteristics by doping ZnO with arsenic (As). ZnO films were deposited onto semi-insulating (001)-GaAs wafers by pulsed laser deposition (PLD). Secondary ion mass spectroscopy (SIMS) showed that As atoms from the GaAs substrate diffused into the ZnO film due to substrate heating during growth.

The acceptor concentrations in the As-doped ZnO films range from 10^{17} to $10^{21}/cm^3$ and Hall mobilities range from 1 to 50 $cm^2/V{\cdot}s$. However, the report lacks strong evidence that the p-type conductivity was not caused by Zn-doped GaAs. The authors admitted that the Hall effect values could have "large uncertainty" and that the interface between GaAs and ZnO was not well understood [33].

Xiong *et al.* [34] reported doping ZnO p-type intrinsically by increasing the chemical potential (partial pressure) of oxygen during reactive sputtering. Hall effect measurements indicate that when the O_2 fraction in the sputtering gas is above 55%, the ZnO films show p-type conductivity. Xiong *et al.*'s results and similar experiments we conducted will be discussed in Chapter 3.

In January, 2002, Eagle-Picher Technologies announced the production of p-type ZnO thin films by molecular beam epitaxy (MBE). Carrier concentrations of $\sim 1\times10^{18}/cm^3$ and mobilities of 2 $cm^2/V{\cdot}s$ were reported for the p-type ZnO thin films [11]. A later article by Look *et al.* [35], which is probably related to the announcement, reported p-type homoepitaxial ZnO films grown by MBE with N_2 as the dopant source. The deposition was enhanced by an RF plasma source, and the films were deposited onto Li-doped semi-insulating ZnO substrates, which were heated from 400 to 750˚C. The hole concentration in the p-type ZnO films is of $9\times10^{16}/cm^3$, the Hall mobility is of 2 $cm^2/V{\cdot}s$, resulting in a resistivity of 40 $\Omega{\cdot}cm$ [35].

1.4 Prediction of p-type doping with NO/NO_2

Among the above p-type results, Joseph *et al*. [32] is the most frequently cited one. The p-type ZnO films were grown by pulsed laser deposition (PLD) from a Ga-pre-

doped ZnO source. N_2O was chosen to be the N source with the intention of suppressing formation of native donors such as Zn_i and V_O with excess oxygen. An electron cyclotron resonance (ECR) plasma was used during deposition to break up N_2O into atomic nitrogen and the films were deposited onto glass substrates, which were pre-heated to 400˚C. Table 1-1 lists the key results from that paper. With Ga as the co-dopant of N, p-type results are attributed to the N-Ga-N complex formed in the ZnO films [32]. Such a complex stabilizes the N atoms on their appropriate sites and reduces the repulsion between the N acceptors. The complex increases the solubility of N acceptor and thus turns the ZnO films p-type.

Dopant	Ga source	ECR	Resistivity	Carrier density	Mobility	Carrier type
			(Ω.cm)	(cm^{-3})	($cm^2/V.s$)	
N_2O	No	No	4.3×10^{-2}	4.5×10^{20}	0.31	n
N_2O	No	Yes	5×10^{5}	**2.0×10^{10}**	**1.9×10^{3}**	p
N_2O	Yes	Yes	2.0	**4×10^{19}**	**0.07**	p
N_2	No	Yes	0.17	1.3×10^{19}	1.3	n

Table 1-1: key results reported in Ref. [32]

Yan *et al*. [36] offered a different explanation for the results shown in Table 1-1. Yan *et al.* suggested that in nitrogen-doped ZnO the relevant defects are substitutional atomic nitrogen on oxygen sites (N_O) and molecular nitrogen on oxygen sites [$(N_2)_O$]. N_O is an acceptor while $(N_2)_O$ is a double shallow donor. A source of atomic N is required to form N_O for p-type doping. As shown in Table 1-1, data from Joseph *et al*. indicate that ZnO samples showed p-type properties only when both N_2O was used as the dopant and the electron cyclotron resonance (ECR) plasma was on. The presence of gallium co-

dopant increased the carrier concentration from 10^{10} to $10^{19}/cm^3$ but led to very low mobility (from 1.9×10^3 to 0.07 $cm^2/V\cdot s$). Yan *et al.* proposed that the ECR plasma breaks down N_2O into NO and N:

$$N_2O \rightarrow NO + N \qquad (1\text{-}1)$$

Yan et al. emphasize that it is NO that forms acceptor defect N_O in ZnO. N, on the other hand, reacts with Ga to form GaN. Formation of GaN shifts the equilibrium in Equation (1-1) towards the right hand side and thus enhances the doping efficiency. However, GaN precipitates and forms undesired defects that reduce the mobility. From the above theory, the key of obtaining p-type doping is providing an atomic nitrogen source. Therefore, NO and NO_2 appears to be more effective dopants than N_2O and could produce p-type ZnO without the presence of Ga as a codopant and an ECR plasma [36].

2. Reactive Sputtering of ZnO in NO_2 plasma

2.1 Sputtering process

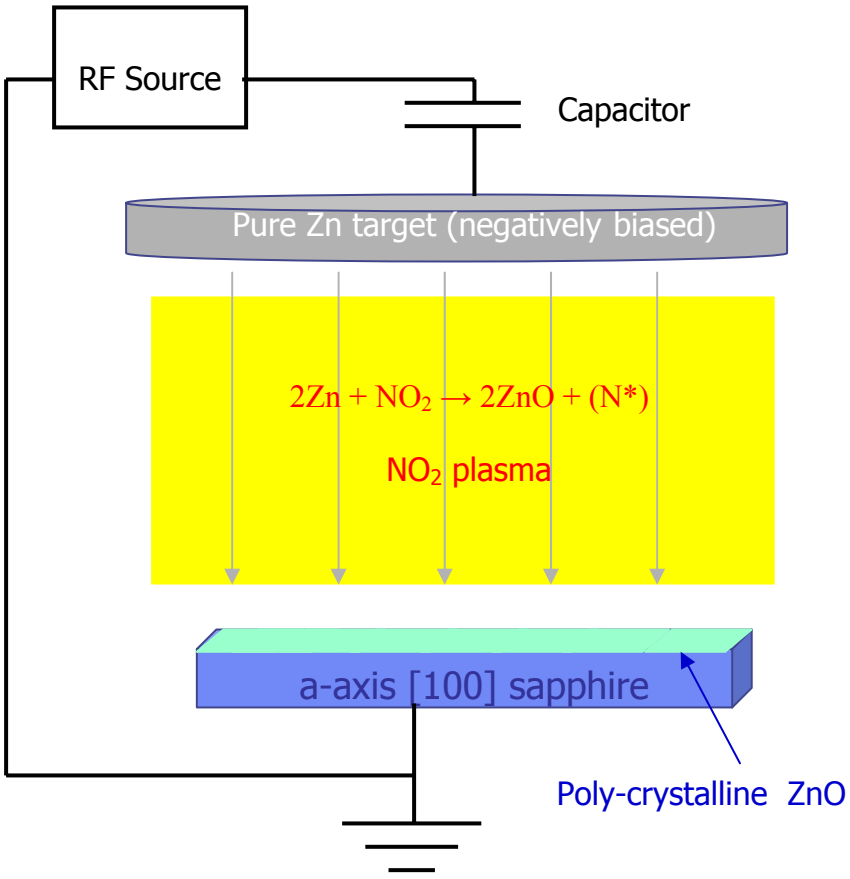

Figure 2-1: Reactive sputtering of ZnO

ZnO thin films are deposited by reactive sputtering in an NO_2 plasma in a Perkin-Elmer 2400 AC diode sputter system in a mechanically pumped stainless steel chamber (Figure 2-1). An 8-inch diameter, pure Zn target and a sapphire substrate are housed in the chamber. In an AC sputtering process, the substrate is electrically grounded while a radio frequency (13.56 MHz) AC voltage is applied to the target. A capacitor is

connected between the RF source and the sputtering system. A specific pressure of gas, in our case about 12 mtorr of NO_2, is maintained during the sputtering process. The strong AC electric field accelerates electrons that collide with NO_2 molecules, ionizing some of the NO_2 molecules and producing more electrons to start a glow discharge (plasma). In the plasma the NO_2 molecules may be cracked into different ionic NO, N, and O species. The ions and electrons bombard the target alternatively as the AC field changes polarity. Since electrons are much lighter and thus have greater mobility than positive ions, the target draws a much higher electron current than ion current under the same potential. Therefore, the capacitor in the circuit is always recharged more rapidly by electron current than ion current. When the AC frequency is sufficiently high (> 1Mhz [37]), the net effect of this inequality of mobility of positive ions and electrons is a negative self-bias of the target. This self-bias is equivalent to a negative "DC offset" of the AC voltage, as shown in Figure 2-2. Since the time dependence of the AC voltage is approximately a sinusoidal function, the DC offset reduces the positive target bias to a very small fraction of the full amplitude. The positively charged nitrogen oxide and nitrogen ions thus have a net acceleration towards the target and bombard the target almost continuously. As the positive ions strike the Zn target, they sputter some of the Zn atoms off and produce more secondary electrons from the target. The Zn atoms fly off the target in random directions and react with the oxygen species to form ZnO; some of the ZnO lands on the substrate, condenses, and forms a thin film.

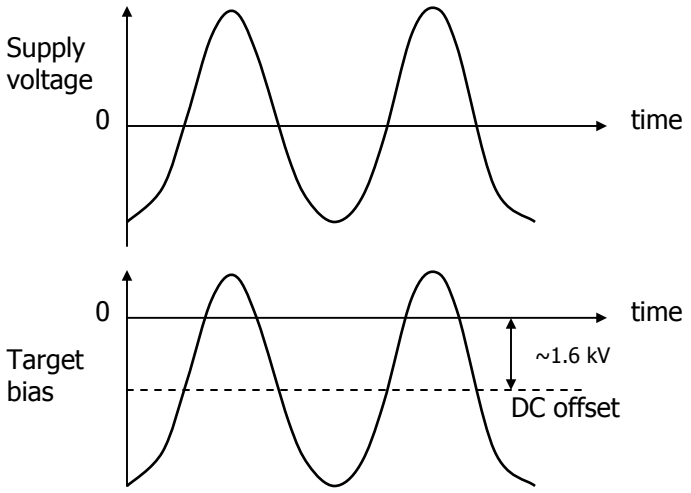

Figure 2-2: Negative self-bias of the target in AC sputtering

Having a high electron affinity, oxygen does not lose electrons easily. Indeed it has a tendency to acquire an extra electron to form a negative oxygen ion (O^-). Electrons and O^- are repelled by the negative bias of the target and are accelerated towards the substrate. Electrons cause more ionization but oxygen ions could bombard the substrate, which can damage the film and reduce the deposition rate [37].

Oxygen bombardment can be reduced by decreasing the negative bias of the target to lower the acceleration or by increasing the gas pressure to reduce the kinetic energy of the oxygen ion by more frequent collisions. However, decreasing the target bias lowers the sputtering rate. Increasing gas pressure reduces the lifetime of atomic nitrogen species since atomic nitrogen species have a strong tendency for combining with each other or with oxygen species. Higher gas pressure reduces the collision path of atomic nitrogen and the average lifetime of the specie. The lifetime of atomic nitrogen should be made as long as possible since p-type doping requires formation of N_O.

Therefore, it is important to find optimum process conditions that balance the oxygen bombardment and the lifetime of nitrogen species.

To maintain a stable plasma in our sputter system, the allowed gas pressure lies between 5 mtorr and 25 mtorr, and the target bias ranges from 1 kV to 2 kV. We found that sputtering in 12 mtorr of NO_2 plasma at 300 Watts (corresponding to 1.6 kV bias offset of the target relative to ground, as shown in Figure 2-2) gives the highest sputter rate at about 10 nm/minute. When the sputtering power and gas pressure deviate from the above values, the sputter rate decreases. Throughout the study we typically sputtered at 12 mtorr and 300 Watts for a period ranging from one-half hour to one hour, obtaining films from 300 nm to 700nm thick.

Due to the toxicity of the NO_2 gas, extra caution has to be taken when delivering it to the sputter machine. A special NO_2 supplying system with all stainless steel gas pipes was built for this purpose. Details of the system can be found in Appendix I.

2.2 Annealing processes

The sputtering machine does not have a heater for the substrate. Growing ZnO films at room temperature is probably disadvantageous for incorporating atomic nitrogen into the oxygen site and for achieving the desired crystallinity. The as-deposited polycrystalline films are generally too resistive to allow Hall effect measurements. Therefore, the films must be annealed to improve crystallinity and to activate the nitrogen dopant. Both furnace annealing and rapid thermal annealing (RTA) were used in our experiments.

Furnace annealing was performed in an argon environment in a Lindberg Blue quartz tube furnace. Typical furnace annealing occurred at temperatures ranging from 600 to 900°C for 1 hour. RTA was performed in an AG Associates Heatpulse 210 RTP system. Inside the system, samples are sandwiched between two silicon wafers in an argon environment. High-intensity tungsten-halogen lamps shine on the wafers, which reach a precisely controlled temperature in seconds. The sample is heated evenly between the two wafers at temperatures ranging from 200°C to 950°C for a short time (typically from 10 seconds to 3 minutes). Compared to conventional oven annealing, RTA was found to be a more convenient and effective process to obtain sufficiently conductive films for Hall effect measurements. More importantly, transient annealing processes have been found to be more effective than furnace annealing in activation of dopant and have been widely used in post-implantation treatments of III-V semiconductors [38,39]. Therefore, the results from RTA-treated samples are discussed more extensively in the following discussion, although measurements of furnace-annealed samples are also presented for comparison. After testing different annealing conditions we found that RTA at 900°C for 10 seconds gives the best result in terms of electronic and optical properties, as will be shown later.

2.3 X-ray Diffraction

The crystallinity of the deposited film and the effect of annealing are studied with powder X-ray diffraction (XRD). Powder XRD is a non-destructive identification technique for powder or polycrystalline samples. During XRD measurement, a beam of monochromatic X-rays is shined on the sample under a certain angle and an X-ray

detector is installed at the same angle but on the reflective side. The detector records a diffracted X-ray signal when certain planes within properly oriented grains satisfy the Bragg condition:

$$n\lambda = 2d\sin\theta \qquad (2\text{-}1)$$

where n is the order of the diffracted beam, λ is the wavelength of the X-ray, d is the inter-planar distance of the diffracting planes, and θ is the angle between the incoming x-ray and the normal of the diffracting planes. During a θ-2θ scan, the incident angle of X-ray beam (θ) rotates simultaneously with the detector angle with respect to the sample while the sample remains stationary. Since the X-ray wavelength λ is known and the diffracting angle θ is shown in the diffraction pattern, from equation [2-1] one can find the lattice parameter d of the diffracting plane. XRD also reflects crystal quality. In a polycrystalline sample, very small crystals have few planes for x-ray to diffract. This, in turn, makes the selection of the exact θ less stringent and leads to a broader peak [40].

The XRD measurements were taken from 5 to 70 degrees with a 0.05-degree step size in a Siemens D5000 diffractometer. The wavelength of the X-ray beam was 1.5406 Å. Figure 2-3 shows the XRD patterns of ZnO films grown in 10% O_2 in Ar. One sample is as-grown while the other is RTA-treated at 900°C for 10 seconds. The XRD pattern of a bare sapphire substrate is also provided. From the wavelength of the X-ray and the diffraction angle all peaks in the diffraction pattern were identified using equation (2-1). In both the as-grown sample and the annealed sample there is a distinct (110) signal. This is due to the sapphire substrate that is a-axis (110) oriented. After rapid thermal annealing at 900˚C for 10 seconds, the (110) signal grew stronger and sharper, and other characteristic peaks emerged. The full-width half-maximum (FWHM) of the (110) peak

decreases from 0.65˚ to 0.40˚ and the integrated intensities increase by 7.19 times (the plots in Figure 2-3 is normalized).

XRD patterns on furnace-annealed samples, which are not shown here, indicate more significant improvement of crystallinity for furnace annealing. After furnace annealing at 900˚C for 1 hr, the FWHM of the (110) peak decrease from 0.75˚ to 0.45˚ and the intensity increases by 75.2 times. Under an optical microscope, large grains of several microns in size are observed in the furnace-annealed samples. In as-deposited films and RTA samples, the optical microscope does not have high enough resolution to determine their grain sizes. In general, the short processing time of RTA (maximum 180 second) is insufficient for extensive grain growth. However, crystallinity of our sample is not the primary concern in this project. A more important goal of the annealing is to activate the nitrogen dopant to form a non-equilibrium defect N_O [35]. From the literature the proper conditions for dopant activation in III-V compounds is typically annealing at 400 – 700°C for 1 – 100 seconds [38,39]. For II-VI compounds probably a higher temperature is required to activate the dopant since II-VI compounds have higher ionicity and thus the dopant could have higher activation energy. The activation time in II-V is expected to be in the same scale as that of III-V compounds. Besides, long time furnace annealing leads to diffusive redistribution of dopants, which is detrimental. In fact, in some N-doped furnace-annealed films nitrogen is observed to form N_2 bubbles inside the films, as will be shown later. Therefore, although furnace annealing provides better crystallinity, RTA is the preferred annealing process for sample annealing in this project.

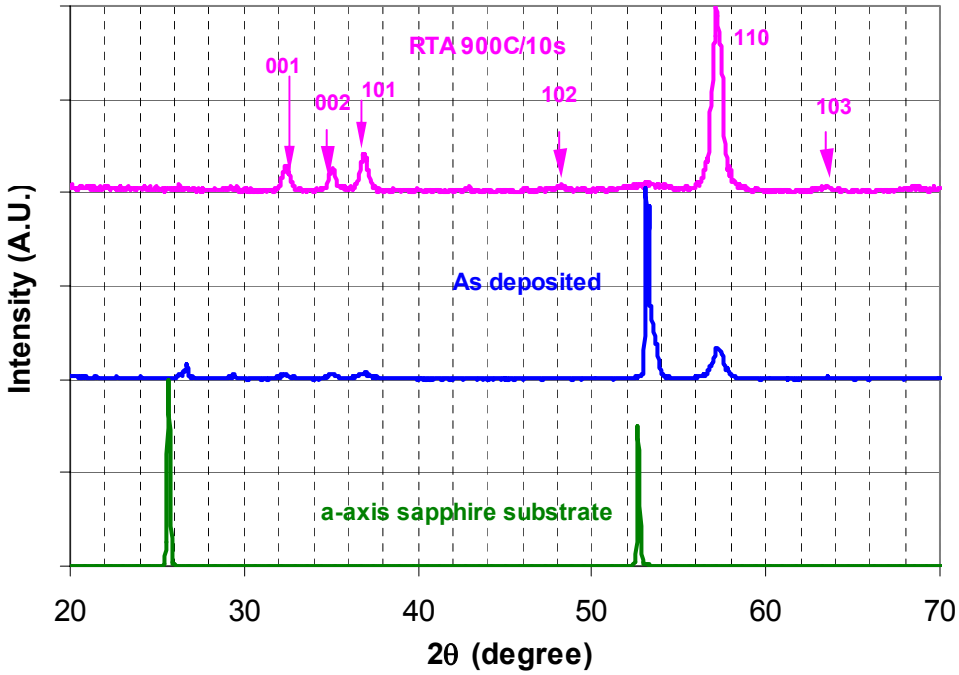

Figure 2-3: XRD of ZnO films and the sapphire substrate

2.4 Hall effect

The carrier type, concentration, and mobility were determined using the Hall effect. In a Hall effect measurement, a magnetic filed is applied perpendicularly to the thin film with a current passed through the film. The Lorentz force creates an internal electric field (Hall field) that is perpendicular to both the current and the magnetic field. Since the magnetic field and current density are known, and the Hall voltage created by the applied magnetic field can be measured, the carrier concentration can be determined by the following equation:

$$n = \frac{Bj}{E_H}, \qquad (2\text{-}2)$$

where n is carrier concentration, j is the applied current density, B is the magnetic field, and E_H is the Hall field. The Hall mobility for the carriers can be calculated from the following correlation:

$$\mu = \frac{1}{en\rho}, \tag{2-3}$$

where μ is mobility, e is the charge of electron, n is carrier concentration, and ρ is the resistivity [41].

The Hall effect measurements were carried out in the van der Pauw (4 points) configuration [42] under direct current ranging from 1mA to 0.01mA in a magnetic field of 3000 Gauss. Details of a typical Hall measurement can be found in Appendix II. Comparison of the Hall effect data of the undoped film (sputtered in 10% O_2/90% Ar) and the N-doped film in Table 2-1 shows that the nitrogen dopant seems to have no significant effect in electronic properties. On the other hand, the data indicate that RTA is more effective in improving the electronic properties. Compared to furnace annealing, the NO_2-doped films after RTA are 57.2 times higher in electron concentrations, 62.4 times lower in resistivity, and 1.2 times higher in mobility. Unfortunately that means a higher donor concentration!

Film	Pressure	Anneal	Conc.	Resistivity	Mobility	Type
	(mtorr)		(cm^{-3})	(Ohm.cm)	(cm^2/Vs)	
Undoped	12	RTA 900°C/10s	$1.01x10^{19}$	0.0574	-10.75	n
		Furnace anneal 900C/1hr in Ar	$2.68x10^{17}$	1.7820	-11.46	n
NO_2 grown	15	RTA 900°C/10s	$1.93x10^{19}$	0.0191	-18.32	n
		Furnace anneal 900°C/1hr in Ar	$3.37x10^{17}$	1.1920	-15.59	n

Table 2-1: Hall effect measurements on undoped and N-doped film

2.5 Photoluminescence and optical absorption

Photoluminescence (PL) spectroscopy suggests that the high electron concentration in RTA-treated, unintentionally doped ZnO samples is due to formation of Zn_i. Furnace annealing of the unintentionally doped ZnO samples leads to formation of V_O, which could behave as an electron trap.

PL spectroscopy is a contactless, nondestructive method of probing the electronic structure of materials. In a PL process, a laser beam is directed onto a sample. If the photon energy of the laser beam is greater than the band gap of the material, the photons are absorbed due to a photo-excitation process, in which electrons in the material are energized into higher allowed states. These excited electrons tend to form electrons-hole pairs with holes formed in the valence band. Such pairs are called excitons. When the excitons recombine, i.e., the electrons return to their equilibrium states, they release energy that is dissipated as emission of photons (radiative process) or other means (non-radiative processes). In the case of photon emission, which is called photoluminescence, the emitted photon energy is related to the difference in the energy of the levels between

the electron states that are involved in the transition. The quantity of photons (signal intensity) is related to the relative contribution of the radiative process.

PL spectroscopy can be used to determine the fundamental bandgap of semiconductors since the most common radiative transition in semiconductors occur between states at the bottom of the conduction band and the top of the valence band. However, since the PL signals come from recombination of excitons, the energies of the PL peaks are slightly smaller than the actual bandgap energy. PL peaks originate from free and trapped exciton emission have different energies. For free excitons, the emission energy is lower than the bandgap by the amount of exciton binding energy. Defect-bound excitons have even lower emission energy due to the binding energy of excitons to the defects. If excitons are bound by a deep state formed by a localized defect, a mid-gap deep level emission is also observed. PL is very sensitive to deep level states [43].

A more reliable way than PL to study the fundamental bandgap is optical absorption. Absorption is the direct measurement of photo-excitation across the bandgap; therefore, it does not have the complication of exciton recombination described above. In an absorption measurement, a beam of monochromatic light with tunable wavelength is shined on a sample, while the intensity of the transmitted light is detected on the backside of the sample. When the photon energy is higher than the bandgap of the material, the light is absorbed more effectively due to the photo-excitation process. If one plots the square of the absorption coefficient as a function of photon energy, the interband excitation appears as a linear absorption edge. The bandgap energy can be determined from the intercept of the absorption edge and the base line.

In the PL spectroscopy setup, the samples were cooled to 10-20K in a closed-cycle He cryostat. The PL signals were generated in a backscattering geometry by excitation with the 325 nm (3.8 eV) line of an Omnichrome Model 100 He-Cd laser with an excitation power of 10 mW. The PL signal was focused and directed into a Spex 1404 0.85m double spectrometer, which has a grating of 1800 groves/mm and is blazed at 400nm. In the monochromator the PL signal was dispersed into a GaAs photomultiplier detector. The optical absorption measurements were performed in a Varian Cary 2390 near-infrared-visible-UV spectrophotometer.

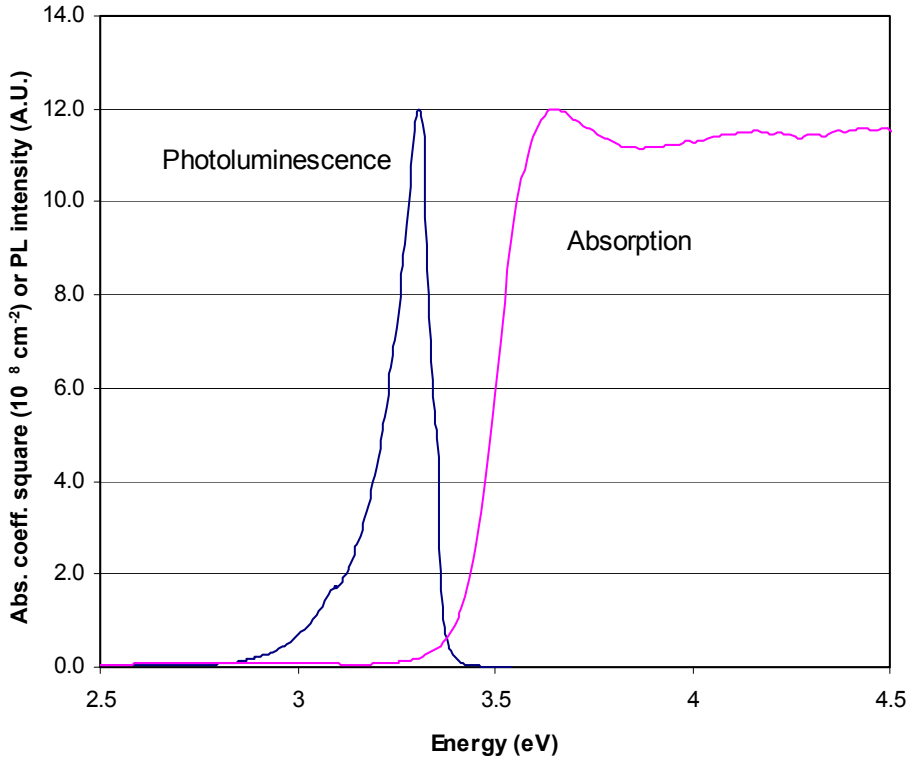

Figure 2-4: PL and optical absorption measurements near the band gap. The sample is undoped and RTA processed at 900°C/10s

Shown in Figure 2-4 is the PL and optical absorption measurements near the bandgap. From the absorption edge the bandgap is determined to be 3.42 eV, while the PL peak is located at 3.31 eV. The difference between PL and absorption (Stokes shift = 110 meV) is much larger than the exciton binding energy (60 meV). In the literature, emissions at ~ 3.31 eV have been previously reported and were attributed to inelastic scattering between excitons [44,45]. The scattering excites one exciton into a higher state (n = 2,3,4,…,∞) while the other exciton is annihilated and emits a photon, whose energy is roughly between 3.318 (n = 2) and 3.303 eV (n = ∞). Therefore, in this case the PL signal at 3.3 eV can be considered as the result of interband emission.

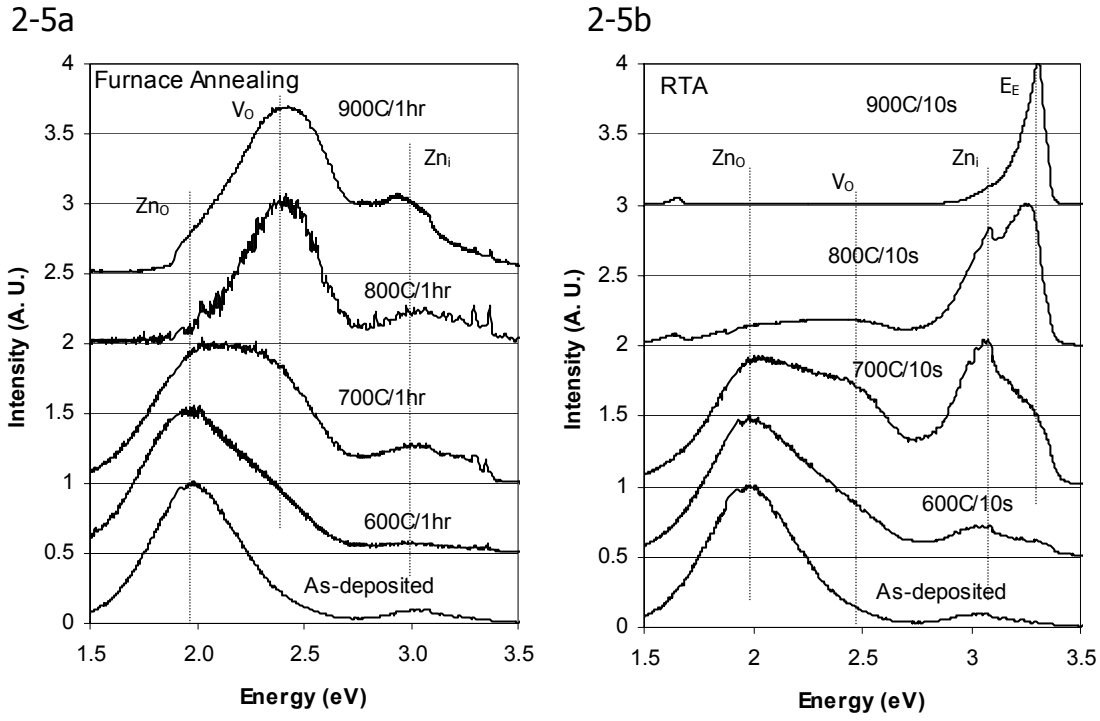

Figure 2-5a and b: Photoluminescence of ZnO films furnace-annealed (a) and rapid thermal annealed (b) at various temperatures

Figure 2-5 shows a number of PL spectra of ZnO films that were furnace-annealed (2-4a) and rapid thermal annealed (2-4b) at various temperatures. All films were cleaved from the same sample that was produced by sputtering in 10% O_2 in Ar. The as-deposited samples have a strong yellow emission (2.0 eV). As the annealing temperature increases, yellow emission weakens and green (2.4 eV) and blue (3.0 eV) emissions appear. The furnace-annealed samples give stronger green emission while the RTA-treated samples give stronger blue emission. At temperatures above 700°C, UV (3.3 eV) emission emerges in RTA-treated samples and dominates the spectrum when the temperature reaches 900°C. Furnace-annealing at 900°C for 1 hour has only very weak phonon-replica-like features at about 3.3 eV but results in strong green emission. In previous reports, the yellow (2.0 eV), green (2.4 eV), and blue (3.0 eV) emissions have been attributed to Zn_O [16], V_O [16, 46, 47], and Zn_i [48], respectively. Calculations [16, 48] have shown Zn_i to be a shallow donor that can be described by the hydrogenic model. Zn_O and V_O are deep donors that have higher ionization energies [16, 46, 47]. Therefore, Zn_i is likely the major donor in our ZnO films. A sketch of the correlations between the PL signals and the native defects is shown in Figure 2-6. The reason for Zn_O to be the dominant defect in the as-deposited films is not clear, but considering the deposition condition (room temperature) is far from thermal equilibrium, it is not surprising that defects with slightly higher formation energies like Zn_O [16] could form. Upon annealing, lower energy defects such as Zn_i and V_O dominate.

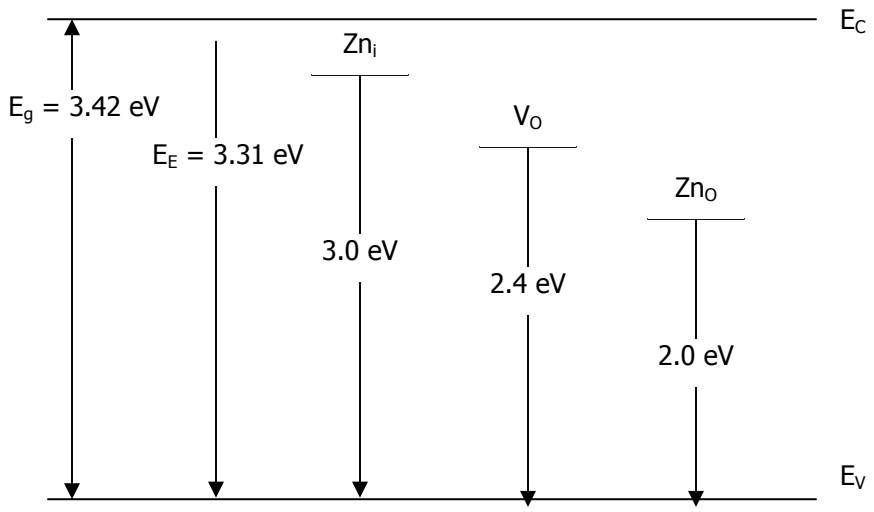

Figure 2-6: Sketch of defects states in ZnO bandgap and their corresponding emission signals

Based on the PL spectra, the high electron concentration in the RTA-treated samples can be attributed to Zn_i. In the furnace-annealed samples, lower electron concentrations than those of the RTA-treated samples can be attributed to both low concentrations of Zn_i and V_O deep-level states, which could behave as electron traps. In an attempt to reduce Zn_i and V_O concentration in unintentionally doped ZnO, we increased the oxygen chemical potential (partial pressure) during deposition. Details of the experiments will be discussed in Chapter 3. It is worth mentioning that we have examined the possibility of hydrogen being the donor source in our films. As mentioned above, 98.8% hydrogen could be driven out by annealing at 600°C for 5 minutes. We annealed RTA-treated samples in an argon environment at 600-700°C for up to 1 hour. However, the electron concentration remains at the low $10^{19}/cm^3$ or high $10^{18}/cm^3$ range in those samples. Therefore, hydrogen is not a major donor source in our samples.

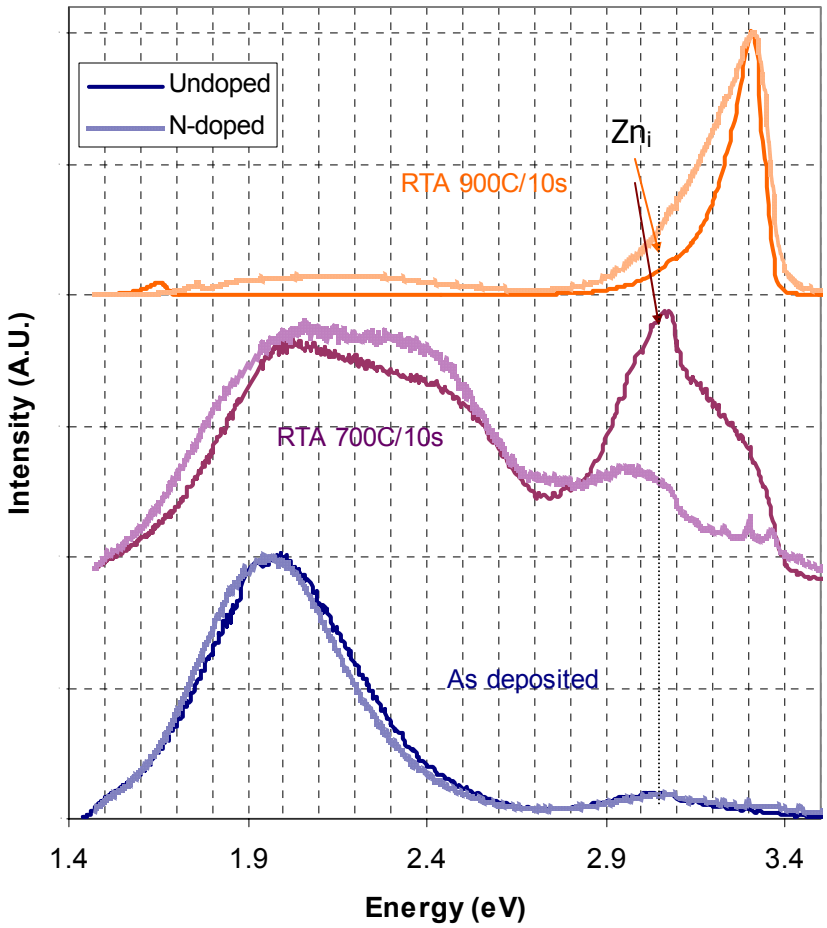

Figure 2-7: Photoluminescence of doped and undoped ZnO annealed at various temperatures.

When nitrogen dopant is introduced, PL spectra show that the formation of Zn_i is suppressed. Shown in Figure 2-7 is the comparison of PL spectra of the undoped and doped samples, rapid thermal annealed at various temperatures. The solid lines represent the same undoped samples shown in Figure 2-3b while dotted lines represent NO_2 grown samples, deposited under similar settings (12 motorr, 300 Watts). The two samples show similar spectra except that the doped samples show very weak blue emission. The suppression of Zn_i could be attributed to the combination with the oxygen species in the

films and/or the occupation of nitrogen dopant in the interstitial sites. However, lower Zn_i concentration does not seem to reduce the electron concentration. The Hall effect measurements given in Table 2-1 indicate that the electron concentrations of the nitrogen-doped samples are comparable to those of the undoped one. After RTA, the electron concentration of the nitrogen-doped sample also reaches $10^{19}/cm^3$, the same as the undoped sample that shows a strong Zn_i signal. One explanation is that the nitrogen dopants in our film actually behave as donors. As mentioned above, $(N_2)_O$ is a double shallow donor. X-ray absorption experiments show that a high concentration of N_2 exists in the nitrogen-doped films, as will be shown later. Besides suppressing the Zn_i signal, the nitrogen dopant also broadens and weakens the interband emission signal after RTA treatment at 900C° for 10 seconds. Spectra in Figure 2-7 are normalized; the broadening effect is clearly shown. N-doping increases the FWHM of the 3.3 eV signal from 0.1138 eV to 0.1896 eV and reduces its intensity by 15.2 times.

2.6 SIMS

To determine the concentration of nitrogen dopant in our film, we used secondary ion mass spectrometry (SIMS). In a SIMS measurement, the surface of the sample is bombarded by primary ions (typically Cs^+, O^-, or O^+), emitting secondary ions. Secondary ions are separated in a mass spectrum analyzer to yield information about the concentrations of specific elements. By digging a flat-bottom crater in the sample surface and analyzing the secondary ions from different depths, one can generate concentration profiles for different elements. Figure 2-8 shows the SIMS profile of a 700nm thick NO_2 grown ZnO film, deposited on an a-axis sapphire substrate. The nitrogen concentration is

quite uniform throughout the depth at about 3×10^{20} atoms/cm^{-3}, which corresponds to 0.3 atomic percent, a very high concentration for a dopant. SIMS data also indicate that the concentration profile remains roughly the same after the rapid thermal annealing process.

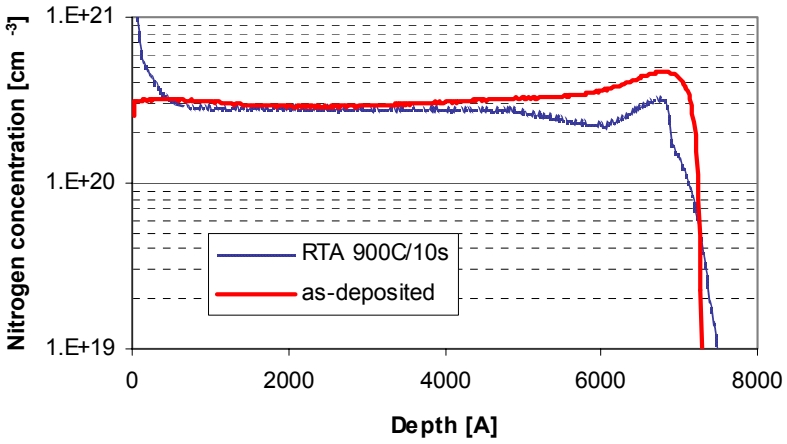

Figure 2-8: Secondary ion mass spectroscopy of nitrogen concentration depth profile

2.7 NEXAFS

The chemical environment of the nitrogen dopant was studied by near-edge X-ray fine structure (NEXAFS). NEXAFS is a non-destructive technique that measures the bonding environment of a specific element by examining the fine oscillation structure near the absorption edge. When X-rays pass through any kind of material, they are partially absorbed and partially transmitted. An X-ray photon with sufficient energy can knock a core-level electron (those in the K, L, and M shell, for example) out of the atom. The process appears in the X-ray absorption spectrum (XAS) as an energy edge at which the absorption rises sharply when the photon energy becomes sufficiently high to remove

an electron in a specific shell. The absorption edges are termed K-, L-, and M-edges after the core shell from which the photoelectron is removed. The energies of the K, L, and M edges are element-specific.

The fine structure beyond the absorption edge in NEXAFS originate from the resonance of X-ray absorption with the excitation of photoelectrons. When an X-ray photon is absorbed, the photoelectron can be excited from a core level to a higher unoccupied molecular orbital. If the photon energy equals the difference between the unoccupied orbital and the core level, the absorption cross-section of X-ray will increase sharply. This appears as a sharp resonance peak in the absorption spectrum. The fine structure of the resonance oscillations, which is very sensitive to the atomic arrangement and the oxidation state of atoms, reflects the local environment of the element. NEXAFS spectroscopy studies the resonance structure within 40 eV above the absorption edge [49]. The fine structure of the K-edge (390 keV) of gaseous nitrogen and various nitrogen oxides have been studied extensively [49-56]; thus, NEXAFS is extremely suitable for studying the bonding environment of nitrogen dopants in our films.

NEXAFS measurements of our ZnO samples were taken in the Advance Light Source (ALS) at the Lawrence Berkeley National Laboratory. The ALS is an electron synchrotron facility that produces soft X-rays and UV radiation. A synchrotron produces soft X-rays and UV light by accelerating an electron beam to travel in a circular vacuum chamber (storage ring) with a speed near the speed of light. When electrons are accelerated, they emit electromagnetic waves. The ALS has 8 straight sections and 8 bends. In some of the straight sections of the storage ring, there are devices called undulators, which contain over one hundred alternating magnetic poles lined up in rows

above and below the electron beam. The magnets force the electrons into a snake-like path. At each turn the electrons are accelerated and emit X-rays, which add up and produce very intense X-ray, also called synchrotron radiation. In our particular end station (beam line 8), the radiation flux is about 10^{12} photons/sec with an energy range of 65 – 1400 eV [50]. During experiments, radiation from an undulator passes through a spherical grating monochromator and a gold mesh filter (for intensity normalization) and is guided to the sample by gold mirrors.

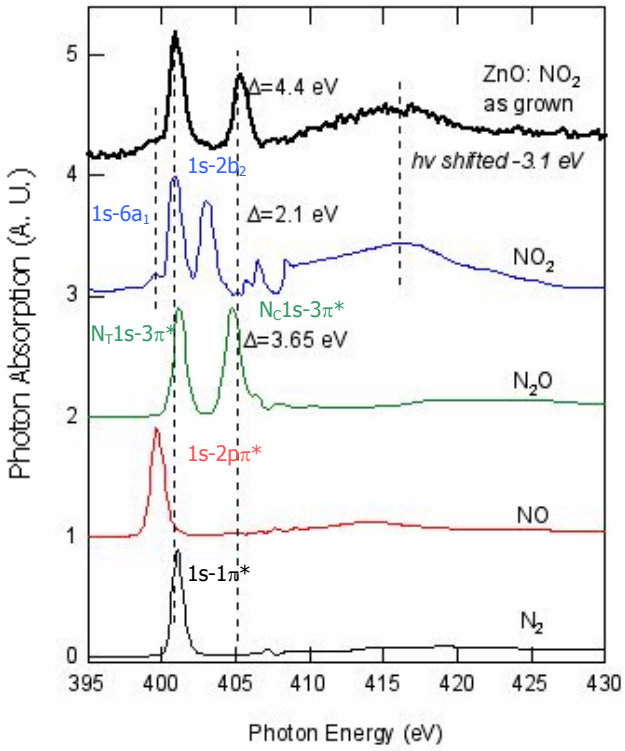

Figure 2-9: X-ray absorption spectra above N-K edge of the as grown N-doped film and all nitrogen oxides.

References:
NO_2: W.H.E Schwartz *et al.* [51]
N_2O: G.R. Wight *et al.* [52]
NO: G.R. Wight *et al.* [53]
N_2: A.P.Hichcock *et al.* [54]

Figure 2-9 shows the absorption spectrum above the N-K edge of the as-deposited film and various nitrogen oxides [51-54]. The sharp peaks in gaseous nitrogen and nitrogen oxides originate from electronic transition from 1s to various π anti-bonding (π*) orbitals as labeled. At higher energy, weaker and broader peaks originate from transition between 1s and σ anti-bonding (σ*) orbitals or multi-electron transition from 1s to π* orbitals [50]. From Figure 2-7, the spectrum of the as-deposited film matches closely with that of N_2O. The molecular structure of N_2O is that a nitrogen atom (sp2 hybridized) at the center with a nitrogen atom and an oxygen atom at each side. The molecule is under constant resonance:

$$N{=}N{-}O \leftrightarrow N{-}N{=}O. \qquad (2\text{-}4)$$

Therefore, the bonds of both nitrogen atoms contain characteristic of π bonding but the two atoms are not equivalent. The lower energy peak at 401 eV corresponds to the 1s - 3π* transition in the terminal nitrogen atom while the higher energy peak at 406 eV corresponds to the 1s - 3π* transition in the center atom. The lower resonance peak in the N-doped ZnO sample also match the 1s - 1π* transition in N_2 and the 1s – $6a_1$ transition in NO_2. However, since in the ZnO sample the 1s – $2b_2$ signal at 403 eV is very weak (1/25 of the peak at 401 eV, almost the same magnitude as the noise), if it is present at all, NO_2 does not exist in high concentrations. As seen in the N_2O spectrum in Figure 2-7, the intensities of the two resonance peaks from the center nitrogen atom and the terminal nitrogen atom are approximately the same, indicating the two atoms have the same X-ray absorption cross-section. On the other hand, in the ZnO spectrum the resonance peak at 401 eV is 1.43 times higher than the peak at 406 eV. This suggests an overlap of the N_2O and the N_2 spectra. From our measurements, the intensity of the 1s - 1π* peak in nitrogen

is 2.18 times that of the 1s - 3π* peak of N_2O. If we assume that the intensity is proportional to concentration, then in the as-deposited film about 83.6% nitrogen exist as N_2O and 16.4% exist as N_2. The main reactions in the plasma during sputtering are actually:

$$3Zn + 2NO_2 \rightarrow 3ZnO + N_2O \quad (2\text{-}5)$$

$$4Zn + 2NO_2 \rightarrow 4ZnO + N_2. \quad (2\text{-}6)$$

Figure 2-8 shows the NEXAFS spectra of the N-doped ZnO sample after RTA treatments at various temperatures, compared with the spectrum of the as-deposited sample. The 1s - 3π* peak at 406 eV becomes weaker and eventually vanishes as the annealing temperature increases. The resonance peak at 401 eV actually increases with annealing temperature and almost doubles after RTA at 900°C for 10 seconds. This indicates that the N_2O dissociates into N_2 at high temperature. This is not surprising since N_2O is an oxidizing agent that decomposes readily upon heating [58]:

$$2N_2O \rightarrow O_2 + 2N_2. \quad (2\text{-}7)$$

The formation of oxygen and nitrogen probably is responsible for the weakening of the Zn_i signal, as shown in Figure 2-7. Zn_i can be oxidized by oxygen and may incorporate into appropriate sites upon annealing. The interstitial sites are then occupied by N_2 and O_2. The formation of O_2, however, does not significantly reduce another native defect V_O. PL spectra of furnace-annealed N-doped ZnO samples, which are not shown, have a strong 2.4 eV signal similar to those in Figure 2-5a. The high electron concentration in RTA treated N-doped ZnO samples is attributed to the formation of $(N_2)_O$, a double shallow donor.

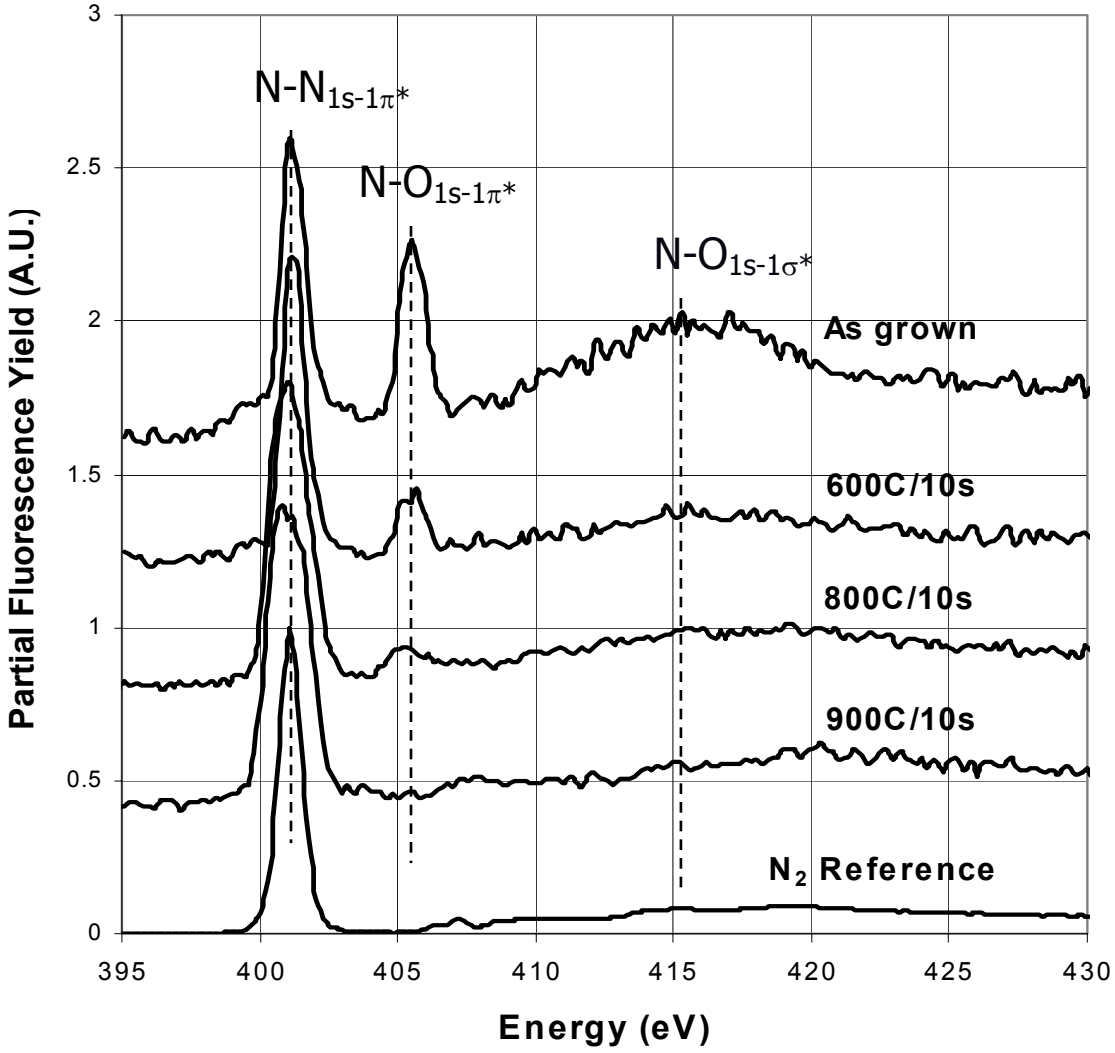

Figure 2-8: NEXAFS study on the effect of rapid thermal annealing

NEXAFS spectra of furnace-annealed samples show similar behavior as those of RTA-treated samples shown in Figure 2-8. However, the furnace annealed N-doped ZnO films do not have comparable electron concentration, which suggests that $(N_2)_O$ does not form in the furnace annealed samples, despite strong 2.4 eV signals indicating high concentrations of V_O. By examining the furnance-annealed samples under an optical microscope, we found fine gaseous bubbles in some of the films that underwent

annealing at 900˚C for 1 hour while no such bubbles were observed in RTA-treated samples. Shown in Figure 2-9a and b is a sample that is N-doped and annealed in an Ar environment at 900°C for 1 hour. The bubbles form clusters in the films, and some bubbles are as large as 10 micrometers in diameter. High-resolution x-ray absorption spectroscopy (XAS) verifies that the bubbles are filled with gaseous nitrogen. Shown in Figure 2-9c are XAS spectra of vibrational structure of the $1s \rightarrow 1\pi_g^*$ transition peak. The data represented by the dotted line was taken with smaller entrance/exit slit widths (15/10 μm) of the spectrometer than those represented by the solid line (40/40 μm) and thus has higher resolution. The spectra match quite well with the absorption spectra of gaseous nitrogen reported in the literature [55,56], as indicated by the 8 arrows in Figure 2-9c. The arrows indicate the energy of the eight vibrational levels of the N $1s \rightarrow 1\pi_g^*$ transition reported in Ref. [55] and [56]. Therefore, upon furnace annealing, N_2 molecules migrate diffusively and agglomerate into bubbles. RTA occurs on a much shorter time scale, which suppresses the redistribution of N_2 and allows formation of $(N_2)_O$. Unfortunately the formation of the $(N_2)_O$ or N_O in the RTA treated samples cannot be verified by NEXAFS because Zn-N and Zn-N_2 bonds are highly ionic and do not resonate effectively during X-ray absorption process.

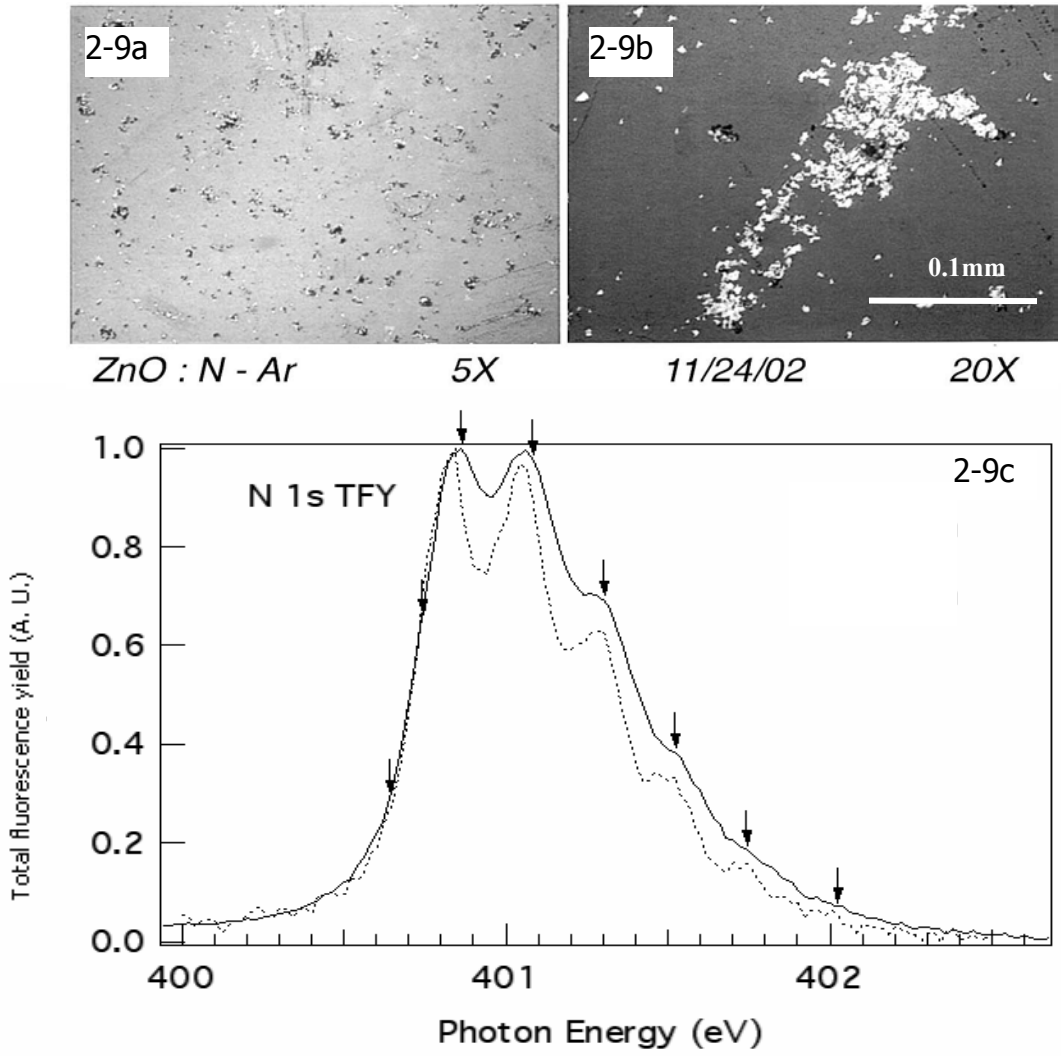

Figure 2-9a and b: Macroscopic bubbles in the furnace-annealed ZnO film under various magnifications; 2-9c: XAS of gaseous phase nitrogen as measured from the macroscopic bubbles. Arrows are from reference [55]

3. Increasing chemical potential of oxygen

3.1 Motivation

As indicated by PL measurements, the high electron concentration in unintentionally doped ZnO is due to the formation of Zn_i. In order to suppress the formation of Zn_i and introduce native acceptors such as V_{Zn} or O_i, one can increase the chemical potential of oxygen in ZnO films. It has been reported that ZnO shows weak p-type conduction upon undergoing heat treatment in atomic oxygen [59]. Recently Xiong *et al* reported the growth of a p-type, undoped ZnO film by increasing the oxygen fraction (in argon) in the reactive sputtering process [34]. The film was deposited in a planar DC magnetron sputtering system with the (001) Si substrate heated to 350˚C. The ratio of O_2 and Ar in the sputtering gas can be adjusted. XRD revealed that the film is polycrystalline but has a primary c-axis orientation. Hall effect data showed that when O_2 fraction is higher than 0.55, the deposited film turns p-type as shown in Figure 3-1. The hole concentration and the film conductivity increase with the the O_2 fraction. By controlling the O_2 fraction during a deposition run, Xiong *et al*. were able to fabricate a p-n homojunction, which was verified by I-V curve measurements. The p-type measurements were attributed to the formation of native acceptors O_i and V_{zn}. Calculations from Ref [34] indicated that increasing the chemical potential of the oxygen in the deposition process increases the formation enthalpy of native donor V_O but lowers the formation energy of O_i and V_{zn}.

Since we have a reactive sputtering system, we can conveniently examine if the above process can be done in our system. Instead of mixing oxygen with argon, which

requires extra flow controllers for adjusting fraction of incoming oxygen, we simply used pure oxygen as the sputtering gas, which would give the highest acceptor concentration according to Xiong's result. The samples were both rapid thermal annealed and annealed in a conventional oven.

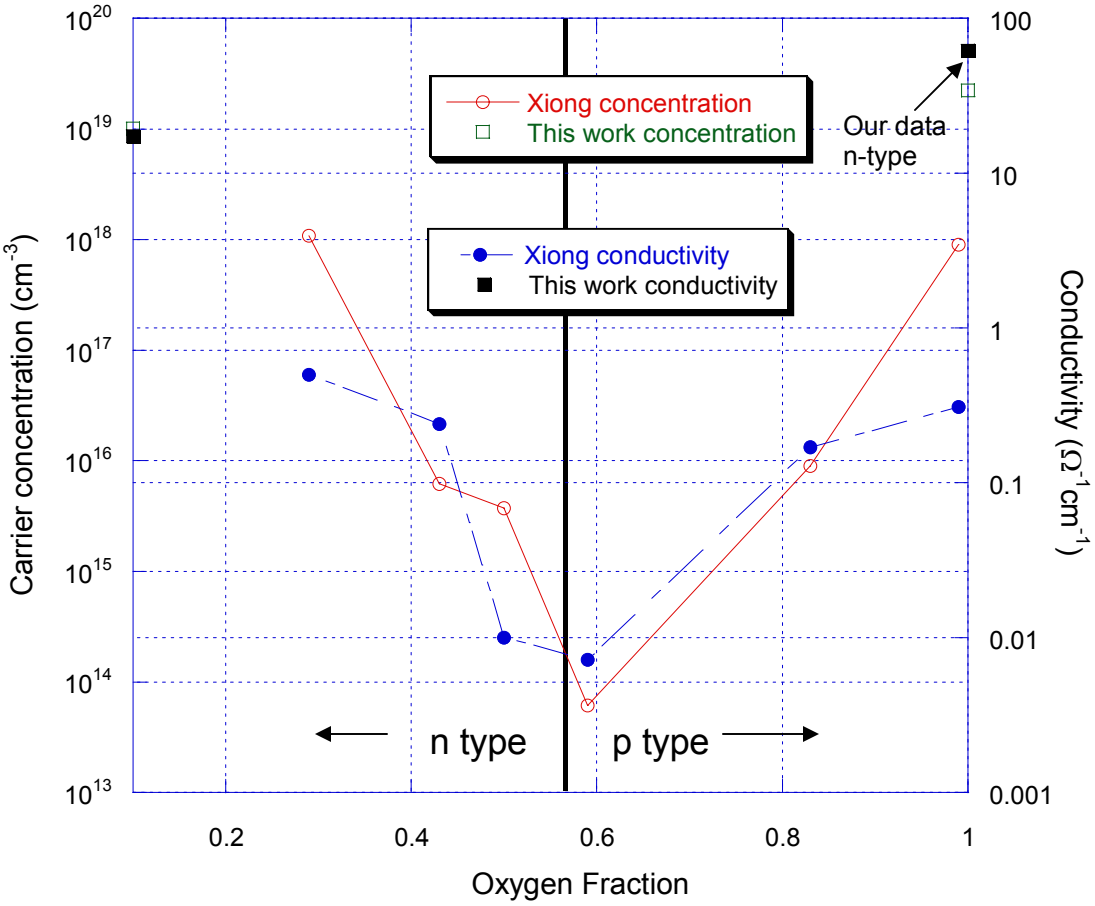

Figure 3-1: Hall effect results from Xiong *et al.* [34] and this work as a function of oxygen fraction during sputtering

3.2 Results and discussions

The Hall effect measurements of the pure oxygen-grown sample are shown in Table 3-1 and are plotted in Figure 3-1. Apparently the oxygen fraction does not have a

significant effect on the electronic properties. Films grown in pure O_2 have similar carrier concentration, resistivity, and Hall mobility as those grown in 10%. If we extrapolate the carrier concentration and conductivity data from Ref [34] to 10% oxygen fraction, the results fall very closed to our data, as shown in Figure 3-1. However, on the oxygen-rich end, the conductivity measurements from Ref [34] turn p-type, while our film remain strongly n-type. The high electron concentration in our 100% O_2-grown ZnO is attributed to formation of the native donor Zn_i. PL spectra of our samples, treated by RTA at various temperatures, are shown in Figure 3-2. The spectra are very similar to those of the 10% O_2-grown samples shown in Figure 2-5b. A strong Zn_i peak at 3.05 eV is observed after RTA at 600-700°C for 10 seconds, indicating that higher oxygen pressure does not suppress formation of the native donors. PL spectra of furnace-annealed samples, which are not shown here, have a strong V_O peak at 2.43 eV. The formation of Zn_i and V_O can be attributed to their low formation enthalpies, even under O-rich condition [16,25].

Oxygen fraction	Pressure (mtorr)	Anneal	Conc. (cm^{-3})	Resistivity (Ohm.cm)	Mobility (cm^2/Vs)	Type
10%	12	RTA 900°C/10s	$1.01x10^{19}$	0.0574	-10.75	n
		Furnace anneal 900C/1hr in Ar	$2.68x10^{17}$	1.7820	-11.46	n
100%	12	RTA 900°C/10s	$2.22x10^{19}$	0.0162	-17.36	n
		Furnace anneal 900°C/1hr in Ar	$3.96x10^{17}$	0.7344	-21.50	n

Table 3-1: Hall effect measurements on films grown in different oxygen fractions

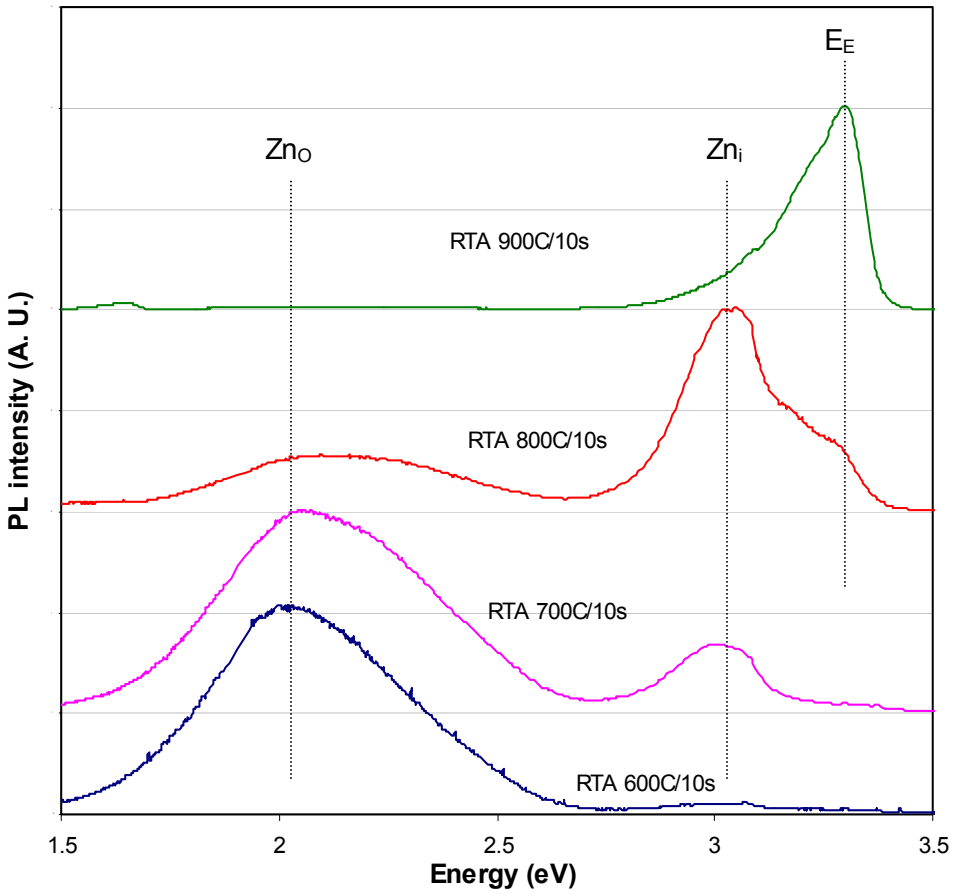

Figure 3-2: PL spectra of O_2-grown ZnO films after RTA at various temperatures.

The different outcome of our experiment from that of Ref [34] is not totally unexpected since our experiment is not a precise repeat. For example, the DC magnetron sputtering system used in Ref [34] is different from the AC diode sputtering system we used. Magnetron sputtering has longer path length for electrons and ions compared to AC diode sputtering. Magnetron sputtering also confines the plasma closer the target, and thus has a higher sputtering rate (Xiong reported a growth rate of up to 167 nm/minute,

while we only have 10 nm/min). In Ref [34] the substrate was heated to 350°C while in our experiment, the substrate remained at room temperature and we have to rely on annealing after deposition to force crystal regrowth. Heating during film growth could promote formation of energetically unfavored native acceptors.

4. Nitrogen ion implantation

4.1 Motivation and experimental setup

As reported in Chapter 2, reactive sputtering of ZnO in NO_2 leads to the incorporation of high concentrations of N_2 and N_2O in the films. Since our goal is to introduce atomic nitrogen substitution N_O, it is important to suppress the recombination of the atomic nitrogen. Another approach is to use nitrogen ion (N^+) implantation to mechanically force atomic nitrogen into the zinc oxide lattice. Ion implantation uses a high voltage accelerator to produce a high velocity, energetic beam of impurity ions. Upon impact the ions are buried below the target's surface. By controlling the accelerating voltage and dose, one can control the concentration and depth of the dopant. Since implantation damages the lattice, the implanted sample needs to be annealed to re-grow the crystal and activate the dopant. Generally RTA is used for post-implantation annealing since the time scale and temperature of RTA is optimized to the activation requirements of the dopants. [38,39]

In our experiments, the implantation targets are 600nm-thick polycrystalline ZnO films sputtered on a-axis oriented sapphire in 10% oxygen backed by argon, oven annealed to give a relative low carrier concentration ($10^{17}/cm^3$). Since the proper dose of N^+ and proper RTA temperature to activate the nitrogen to become N_O are not known, samples were implanted with three different doses (10^{14}, 10^{15}, and $10^{16}/cm^2$) and part of these samples were RTA treated at temperature ranging from 600°C to 900°C. The implantation energy of the N^+ was 120 keV, which gives approximately a Gaussian distribution with the maximum at a depth of about 100 nm based on computer

simulations with *Ion Beam Profile Code* Version 3.20 by Implanted Science Corp. The maximum volume dopant concentrations are about 5 x $10^{18}/cm^3$, 5 x $10^{19}/cm^3$, and 5 x $10^{20}/cm^3$ for the three doses, respectively.

4.2 Results and discussions

Figure 4-1 shows the electron concentration of the implanted samples as a function of RTA temperatures. Also shown are the electron concentrations of the unimplanted samples for comparison. Apparently N^+ implantation results in higher electron concentrations. As shown in Figure 4-1, samples with higher doses of nitrogen have higher carrier concentrations, although the carrier concentration is not proportional to the dose. After RTA at 600°C for 10 seconds, electron concentrations are higher by 11.3, 8.75, and 44.4 times in the 10^{14}, 10^{15}, and $10^{16}/cm^2$ samples, respectively, as compared to the unimplanted samples. At a higher RTA temperature, the electron concentration increases, and the effect of the implantation is less pronounced. After RTA at 900°C for 10 seconds, electron concentration is higher by 1.44, 2.11, and 3.04 times, respectively.

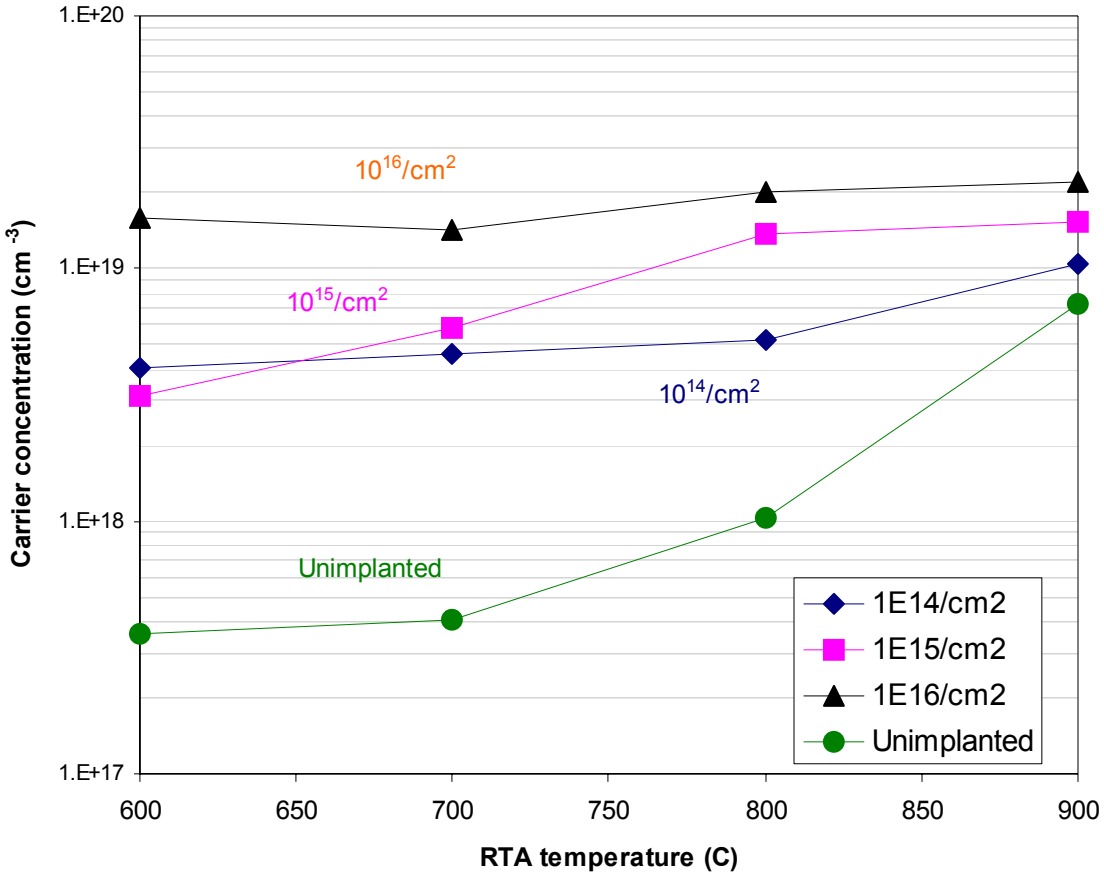

Figure 4-1: Electron concentrations of N^+ implanted ZnO films as function of RTA temperature. Also shown are carrier concentrations of unimplanted films for comparison

If the acceptor N_O forms in the ZnO films, it could be compensated by Zn_O [26], as discussed in Chapter 1. Zn_O appears as yellow emission at 2.0 eV in the PL spectra of RTA treated films, as shown in Figure 4-2 a and b. The increase in electron concentration in N^+ implanted films can be attributed to the formation of the donor defect $(N_2)_O$, the defects created by the implantation damage, and the formation of Zn_i upon annealing. Zn_i appears as blue emission at 3.0 eV in the PL spectra. Samples implanted with $10^{14}/cm^2$ have a maximum volume nitrogen (single N) concentration of $5 \times 10^{18}/cm^3$ while the electron concentration is $4.02 \times 10^{18}/cm^3$ after RTA at 600°C for 10 seconds. Therefore,

the formation of the donor defect $(N_2)_O$ cannot alone explain the high electron concentration. Another possible source of free electrons is the defects introduced by implantation damage. Samples implanted with $10^{16}/cm^2$ have a higher maximum nitrogen concentration of $5 \times 10^{20}/cm^3$, and the electron concentration is $1.60 \times 10^{19}/cm^3$ after RTA at 600°C for 10 seconds. It is unclear whether $(N_2)_O$ or implantation damage or both are responsible for the high electron concentration. Considering the high N dopant concentration, it is possible for nitrogen to combine and form high concentrations of $(N_2)_O$. On the other hand, higher implantation dose means higher defect concentration due to implantation damage.

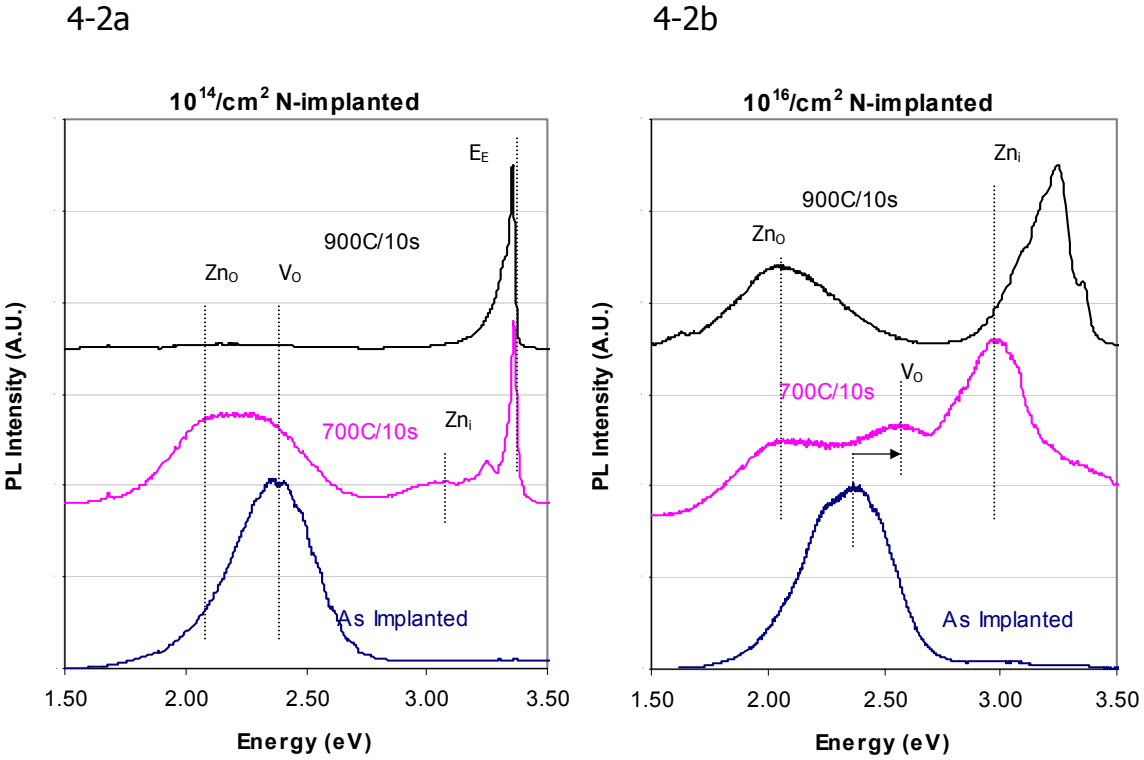

Figure 4-2: PL spectra (13K) of N^+-implanted samples, RTA treated at different temperatures.

Figure 4-2a and b show the PL spectra of the samples implanted with the lowest dose ($10^{14}/cm^3$) and the highest dose ($10^{16}/cm^3$), RTA treated at various temperatures. Since the samples have been furnace-annealed at 900°C for 1 hour prior to implantation, the as-implanted samples give strong green emission at 2.4 eV, which is attributed to the native defect V_O. As shown in Figure 4-2a, upon RTA at 700°C for 10 seconds, the sample implanted with $10^{14}/cm^3$ N^+ gives yellow emission at 2.0 eV (Zn_O), green emission at 2.4 eV (V_O), a weak blue signal at 3.0 eV (Zn_i), and strong interband emission at 3.3 eV. After RTA at 900°C for 10 seconds, the PL spectrum is dominated by the interband emission. Higher implantation doses apparently lead to greater degradation

of the optical properties of the film. As shown in Figure 4-2b, after RTA at 700°C for 10 seconds, the sample implanted with $10^{16}/cm^3$ N^+ generates yellow emission at 2.0 eV, green emission at 2.6 eV (could be the 2.4 eV peak shifted by overlapping with the stronger 3.0 eV peak), and blue emission at 3.0 eV. Strong 3.0 eV emission indicates a high concentration of the native donor Zn_i. After RTA at 900°C for 10 seconds, a broad and weak interband emission at 3.3 eV appears. Weaker interband emission compared to that of the $10^{14}/cm^3$ N^+ implanted samples indicates that higher implantation dose deteriorates both crystallinity and optical properties.

Conclusions

To summarize, polycrystalline ZnO thin films were grown by reactive sputtering. Nitrogen was introduced into the films by reactive sputtering in an NO_2 plasma or by N^+ implantation. All ZnO films grown show n-type conductivity. In unintentionally doped ZnO films, the n-type conductivities are attributed to Zn_i, a native shallow donor. In NO_2-grown ZnO films, the n-type conductivity is attributed to $(N_2)_O$, a shallow double donor. In NO_2-grown ZnO films, 0.3 atomic % nitrogen was found to exist in the form of N_2O and N_2. Upon annealing, N_2O decomposes into N_2 and O_2. In furnace-annealed samples N_2 redistributes diffusively and forms gaseous N_2 bubbles in the films.

Unintentionally doped ZnO films were grown at different oxygen partial pressures. Zn_i was found to form even at oxygen-rich condition and led to n-type conductivity. N^+ implantation into unintentionally doped ZnO film deteriorates the crystallinity and optical properties and leads to higher electron concentration. The free electrons in the implanted films are attributed to the defects introduced by implantation and formation of $(N_2)_O$ and Zn_i.

Although today there is still no reliable means to produce good quality, stable p-type ZnO material, ZnO remains an attractive material with potential for high performance short wavelength optoelectronic devices. One may argue that gallium nitride was in a similar situation a decade ago. Although we did not obtain any p-type conductivity, we hope our research will provide a valuable reference to the literature.

Appendix I. NO_2 supply system for the sputter machine

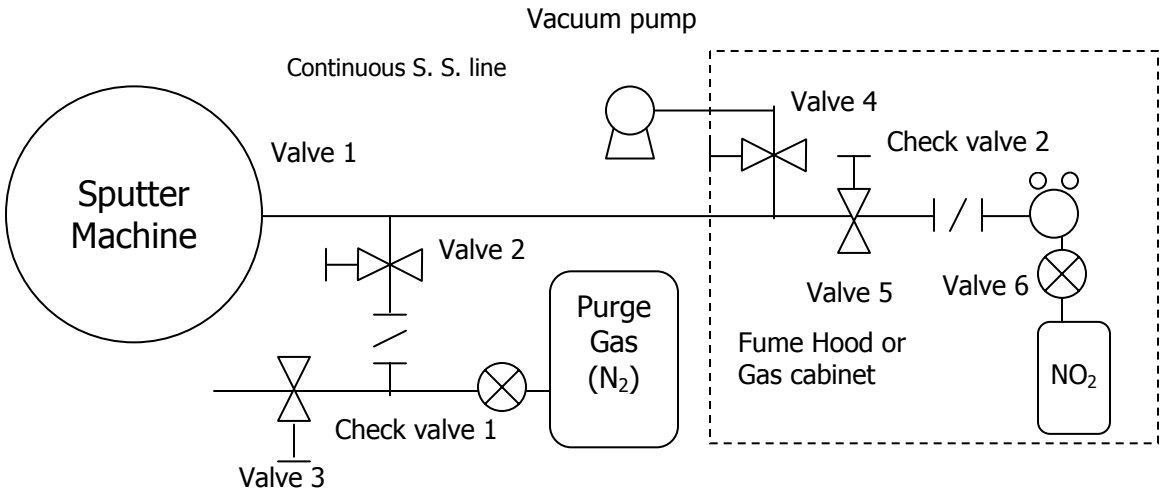

Figure I-1: NO_2 gas supply system for the sputter machine

Figure I-1 is a sketch of the gas supply system for the reactive sputtering experiment. The system was designed to supply nitrogen dioxide (NO_2) for an AC diode sputtering system. Pure NO_2 (99.5%) is stored in a size 6P gas cylinder (4 in. x 8 in., which contains 1 lb. NO_2, corresponding to 8.5 cubic feet of gas at STP). NO_2 is in its liquid form and is not pressurized. Since NO_2 is a very toxic and corrosive gas, the gas cylinder is mounted inside a fume hood and connected to the sputtering system through 1/8" I.D. stainless steel gas pipe. All exhaust goes to either a fume hood or a dedicated vacuum exhaust line.

Before operation, the gaslines are first pumped to a low pressure, and then Valve 4 is open to release NO_2 into the pipeline. During deposition, a small amount of NO_2 (less than 10 cc/minute) continuously flows into the sputter machine, which is maintained under vacuum of about 12 mtorr. The experiment usually runs for 30 minutes to 1 hour.

After deposition, the gas valve in the sputtering machine is first shut and the turbo pump of the sputtering machine will pump most of the NO_2 out of its chamber. The gas line is then pumped to a low pressure, and then Valve 2 is opened to purge nitrogen gas into the system. The above operation procedure makes sure no NO_2 escapes into the atmosphere and no NO_2 remains in the pipeline for an extensive period of time.

Appendix II. Hall effect measurement

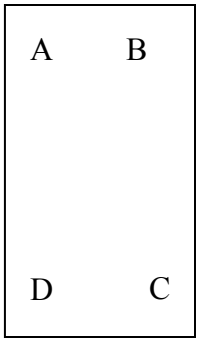

Figure II-1: van der Pauw configuration. A, B, C, and D are In press-on contacts

Shown below as an example is a complete set of original data of Hall effect measurements of a nitrogen-doped ZnO sample, sputtered in 15 mtorr of NO_2 plasma for one hour. The film is 698nm thick as calculated from the weight difference before and after deposition.

Measurements were carried out in the van der Pauw configuration [42]. The van der Pauw configuration is suitable for flat sample of constant thickness and of arbitrary shapes, assuming the contacts are sufficiently small. The film must be uniform and singly

	B field (G)	**Current (A)**		1.00E-03		5.00E-03		5.00E-04	
	3000Gauss			(Amp)		(Amp)		(Amp)	
Measure		current	voltage	Volts (mV)	Std. Dev.	Volts (mV)	Std. Dev.	Volts (mV)	Std. Dev.
ρ		+, B-A	C-D	97.3076	2.00E-03	387.26	2.65E-02	48.60	3.33E-03
		-, B-A	C-D	-97.6827	3.11E-03	-387.37	1.86E-02	-48.96	2.49E-03
		+, D-C	A-B	97.3338	3.48E-03	337.83	1.53E-02	48.64	2.19E-03
		-, D-C	A-B	-97.6644	3.38E-03	-338.06	3.48E-02	-48.94	1.31E-03
		+, C-B	D-A	34.3211	1.22E-03	145.46	1.16E-02	17.09	3.28E-03
		-, C-B	D-A	-34.5185	3.52E-03	-145.55	7.87E-03	-17.30	3.41E-03
		+, A-D	B-C	34.3684	2.19E-03	133.10	5.07E-03	17.14	4.21E-03
		-, A-D	B-C	-34.4645	3.58E-03	-133.18	6.95E-03	-17.24	1.23E-03
Hall	B+	+, C-A	D-B	-63.0662	2.82E-03	-224.40	1.05E-02	-31.66	2.16E-04
	B+	-, C-A	D-B	62.8359	1.40E-03	223.88	2.32E-02	31.41	2.73E-04
	B+	+, D-B	A-C	63.1047	3.72E-03	222.90	1.25E-02	31.57	2.94E-03
	B+	-, D-B	A-C	-63.2954	1.51E-03	-223.10	2.27E-02	-31.76	2.50E-03
	B-	+, A-C	D-B	63.0901	2.71E-03	224.93	1.85E-02	31.55	2.80E-03
	B-	-, A-C	D-B	-63.3171	1.27E-03	-225.12	2.26E-02	-31.80	2.74E-03
	B-	+, B-D	A-C	-63.0486	2.65E-03	-222.57	1.60E-02	-31.66	3.05E-03
	B-	-, B-D	A-C	62.8774	3.98E-03	222.00	6.47E-03	31.46	6.71E-05

Table II-1: Hall effect raw data of a nitrogen-doped ZnO sample

connected (i.e., has no holes). As drawn in Figure II-1, our samples can be approximated to have a rectangular shape. Indium press-on contacts are put on four corners of the sample, which are labeled A-D clockwise.

1.00E-04		5.00E-05		5.00E-06		1.00E-05	
(Amp)		(Amp)		(Amp)		(Amp)	
Volts (mV)	Std. Dev.	Volts (mV)	Std. Dev.	Volts (mV)	Std. Dev.	Volts (mV)	Std. Dev.
9.593	3.77E-03	4.690	1.85E-04	0.2930	1.26E-03	0.7658	1.04E-03
-9.955	2.01E-03	-5.086	2.69E-03	-0.6792	4.13E-03	-1.1895	2.61E-03
9.611	2.57E-03	4.738	3.41E-03	0.3322	2.78E-03	0.8151	3.13E-03
-9.945	1.66E-03	-5.037	1.55E-03	-0.6477	2.80E-03	-1.1294	4.12E-03
3.324	2.65E-03	1.602	1.97E-03	0.0531	8.37E-05	0.2295	4.35E-03
-3.545	2.55E-03	-1.830	9.24E-04	-0.2925	4.20E-03	-0.4534	1.96E-03
3.383	2.52E-03	1.659	2.46E-03	0.1309	3.18E-03	0.2985	1.73E-03
-3.479	2.74E-03	-1.772	1.53E-03	-0.2085	1.78E-03	-0.3885	2.14E-04
-6.466	2.04E-03	-3.294	3.57E-03	-0.4518	3.04E-03	-0.7531	1.66E-03
6.194	2.87E-03	3.033	3.77E-04	0.1802	2.13E-03	0.5124	1.48E-03
6.248	3.76E-03	3.081	3.38E-03	0.2267	2.00E-03	0.5480	1.57E-03
-6.466	2.90E-03	-3.279	3.03E-03	-0.4119	2.76E-03	-0.7253	1.20E-03
6.228	2.99E-03	3.062	5.87E-03	0.1860	6.08E-03	0.5209	6.08E-03
-6.485	2.44E-03	-3.290	2.58E-03	-0.4538	1.13E-03	-0.7533	3.07E-03
-6.437	3.43E-03	-3.251	1.25E-03	-0.4060	3.39E-03	-0.7246	2.43E-03
6.232	2.56E-03	3.076	4.12E-03	0.2293	2.46E-03	0.5460	2.83E-03

Table II-1 (continued): Hall effect raw data of a nitrogen-doped ZnO sample

Table II-1 contains all data taken in a Hall effect measurement. Each row represents a configuration of measurement. The first eight rows of measurements are for the resistivity of the sample, while the next eight are Hall measurements taken in a magnetic field of ~2800 Gauss. Averaging different configurations compensates for the irregularity of the sample shape. The columns represent different currents that passed through the sample.

Trial	Temp	Conc.	Conc.	Resistivity	Rest. Err.	B-Field	Current	Mobility	Mobility
	(K)	(cm-3)	Err.	(Ohm.cm)		(Gauss)	(A)	(cm^2/Vs)	Err.
1	296.56	2.19E+19	1.70E+17	0.0191	1.50E-07	2800	1.00E-03	14.91	0.12
2	296.59	2.21E+19	3.19E+17	0.0191	2.58E-07	2800	5.00E-03	14.78	0.21
3	296.59	2.19E+19	2.83E+17	0.0192	2.93E-07	2800	5.00E-04	14.85	0.19
4	296.56	2.22E+19	1.90E+18	0.0192	1.34E-06	2800	1.00E-04	14.69	1.26
5	296.56	1.83E+19	3.02E+18	0.0192	2.13E-06	2800	5.00E-05	17.80	2.94
7	296.59	9.68E+18	7.88E+18	0.0191	2.93E-05	2800	5.00E-06	33.71	27.45
8	296.56	1.87E+19	1.36E+19	0.0191	1.41E-05	2800	1.00E-05	17.47	12.68
Average		**1.93E+19**	**3.88E+18**	**0.0191**	**6.79E-06**			**18.32**	**6.41**

Table II-2: Results of Hall effect and average values

Based on the raw data from Table II-1, the resistivity, carrier concentrations, and mobility are calculated with Equation (2-2) and (2-3) and are averaged. The results are summarized in Table II-2.

References:

[1] C.H. Mathwson, *Zinc – The Science and Technology of the Metal, Its Aolloys and Compounds*, Reinhold Publishing Corporation, New York (1959).

[2] Frank Porter, *Zinc Handbook – Properties, Processing, and Use in Design*, Marcel Dekker, Inc. (1991).

[3] F.A. Selim, T.K. Gupta, P.L. Hower, and W.G. Carlson, Journal of Applied Physics, **51**, 765 (1980).

[4] D.L Denburg and F.A. Vannatta, IEEE Transactions on Sonics & Ultrasonics, **SU17**, 60, (1970).

[5] W.B. Pennebaker and J.F. O'Hanlon, Journal of Applied Physics, **45** 1315 (1974).

[6] L.R. Weisberg, C.F. Grain, and R.R. Addiss Jr., Applied Physics Letters, **27**, 440 (1975).

[7] H. Shen, J. Pamulapati, M. Taysing, M.C. Wood, R.T. Lareau, M.H. Ervin, J.D. Mackenzie, C.R. Abernathy, S.J. Pearton, F. Ren, and J.M. Zavada, Solid-State Electronics, **43**, 1231 (1999).

[8] G. Zorpette, IEEE Spectrum, **39**, 70 (2002).

[9] T.D. Thompson, Semiconductor Science & Technology, **6**, 1015 (1991).

[10] H. Morkoc, S. Strite, G.B. Gao, M.E. Lin, B. Sverdlov, M. Burns. Journal of Applied Physics, **76**, 1363 (1994).

[11] Eagle-Picher Technologies, 200 BJ Tunnell Blvd., Miami, OK 74354. The announcements are from http://www.epi-tech.com/, as of July 2003.

[12] E. Mollwo, in *Semiconductors: Physics of II-VI and I-VII Compounds, Semimagnetic Semiconductors*, Vol. **17**, edited by O. Madelung, M. Schulz, and H. Weiss (Springer, Berlin, 1982), of *Landolt-Börnstein New series*, p.35.

[13] K. I. Hagemark, Journal of Solid State Chemistry, **16**, 293 (1976).

[14] D. C. Look, J. W. Hemsky, and J. R. Sizelove, Physics Review Letter, **82**, 2552 (1999).

[15] T. Minami, H. Sato, H. Nanto, and S. Takata, Japanese Journal of Applied Physics, **24**, L781 (1985).

[16] S. B. Zhang, S.-H. Wei, and Alex Zunger, Physical Review B, **63**, 075205 (2001).

[17] Y. Chen, D.M. Bagnall, Z. Zhu, T. Sekiuchi, K. Park, K. Hiraga, T. Tao, S. Koyama, M.Y. Shen, and T. Goto, Journal of Crystal Growth, **181**, 165 (1997).

[18] K. Vanheusden, C.H. Seager, W.L. Warren, D.R. Tallant, J.A. Voigt, and B.E. Gnade, Journal of Applied Physics, **79**, 7983 (1996).

[19] Chris Van der Walle, Physical Review Letters, **85**, 1012 (2000).

[20] D. G. Thomas and J. J. Lander, Journal of Chemical Physics, **25**, 1136 (1956).

[21] S. Kohiki, M. Nishitani, T. Wada, and T. Hirao, Applied Physics Letters, **64**, 2876 (1994).

[22] S. J. Baik, J. H. Jang, C. H. Lee, W. Y. Cho, and K. S. Lim, Applied Physics Letters, **70**, 3516 (1997).

[23] Bertrand Theys, Vincent Sallet, François Jomard, Alain Lusson, Jean-François Rommeluère, and Zéphyrin Teukam, Journal of Applied Physics, **91**, 3922 (2002).

[24] K. Ip, M. E. Overberg, Y. W. Heo, D. P. Norton, and S. J. Pearton, Applied Physics Letters, **81**, 3996 (2002).

[25] Fumiyasu Oba, Shigeto R. Nishitani, Seiji Isotani, Hirohiko Adachi, and Isao Tanaka, Journal of Applied Physics, **90**, 824 (2001).

[26] Eun-Cheol Lee, Y.-S. Kim, Y.-G. Jin, and K.J. Chang, Physical Review B, **64**, 058120 (2001).

[27] Eun-Cheol Lee, Y.-S. Kim, Y.-G. Jin, and K.J. Chang, Physica B, **308-310**, 912 (2001).

[28] C.H. Park, S.B. Zhang, and Su-Huai Wei, Physical Review B, **66**, 073202 (2002).

[29] R.M. Park, M.B. Troffer, and C. M. Rouleau, Applied Physics Letters, **57**, 2127 (1990).

[30] Kazunori Minegishi, Yasushi Koiwai, Yukinobu Kikuchi, Koji Yano, Masanobu Kasuga, and Azuma Shimizu, Japanese Journal of Applied Physics, **36**, L1453 (1997).

[31] Tetsuya Yamamoto and Hiroshi Katayama-Yoshida, Japanese Journal of Applied Physics, **38**, L166 (1999).

[32] Mathew Joseph, Hitoshi Tabata, and Tomoji Kawai, Japanese Journal of Applied Physics, **38**, L1205 (1999).

[33] Y. R. Ryu, S. Zhu, D. C. Look, J. M. Wrobel, H. M. Jeong, H. W. White, Journal of Crystal Growth, **216**, 330 (2000).

[34] Gang Xiong, John Wilkinson, Brian Mischuk, S. Tuzemen, K.B. Ucer, and R.T. Williams, Applied Physics Letters, **80**, 1195 (2002).

[35] D.C. Look, D.C. Reynolds, C.W. Litton, R.L. Jones, D.B. Eason, and G. Cantwell, Applied Physics Letters, **81**, 1830 (2002).

[36] Yanfa Yan and S. B. Zhang, Physical Review Letters, **86**, 5723 (2001).

[37] Brian Chapman, *Glow Discharge Process – Sputtering and Plasma Etching*, John Wiley & Sons (1980).

[38] D. Eirug Davies, MRS Symposium Processing, **45**, 261 (1985).

[39] S. J. Pearton, Solid State Phenomena, **1&2**, 247 (1988).

[40] B. D. Cullity, *Elements of X-ray Diffraction*, 2nd Ed. Addison-Wesley Publishing Company, Inc. (1978).

[41] D. K. Schroder, *Semiconductor Material and Device Characterization*, 2nd Edition, John Wiley & Sons, New York (1998).

[42] L.J. van der Pauw, Philips Research Reports, **13**, 1 (1958).

[43] G.D. Gilliland, *Photoluminescence Spectroscopy of crystalline semiconductors*, Material Science and Engineering R: Reports, Elsevier Science S. A. (1997).

[44] D. M. Bagnall, Y. F. Chen, Z. Zhu, T. Yao, M. Y. Chen, T. Yao, and A. Kasuya, Applied Physics Letter, **75**, 469 (1997).

[45] P. Zu, Z. K. Tang, G. K. L. Wong, P. Yu, M. Kawasaki, A. Ohtomo, H. Koinuma, and Y. Segawa, Solid State Communications, **103**, 459 (1997).

[46] M. Liu, A. H. Kitai, P. Mascher, Journal of Luminescence, **54**, 35 (1992).

[47] K. Vanheusden, C. H. Seager, W. L. Warren, D. R. Tallant, J. A. Voigt, Applied Physics Letters, **68**, 403 (1996).

[48] Bixia Lin, Zhuxi Fu, and Yunbo Jia, Applied Physics Letters, **79**, 943 (2001).

[49] Joachim Stöhr, *NEXAFS Spectroscopy*, Springer-Verlag Berlin Heidelberg (1992).

[50] Advanced Light Source, Lawrence Berkeley National Laboratory, 1 Cyclotron Road, Berkeley, CA 94720. The numbers are from http://www-als.lbl.gov, as of July, 2003.

[51] W.H.E. Schwartz, T.C. Chang, and J.P. Connerade, Chemical Physics Letters, **49**, 207 (1977).

[52] G.R. Wight and C.E. Brion, Journal of Electron Spectroscopy and Related Phenomena, **4**, 313 (1974).

[53] G.R. Wight and C.E. Brion, Journal of Electron Spectroscopy and Related Phenomena, **3**, 191 (1974).

[54] A.P. Hitchcock and C.E. Brion, Journal of Electron Spectroscopy and Related Phenomena, **18**, 1 (1980).

[55] G.C. King, F.H. Read, M. Tronc: Chem. Phys. Lett. **52**, 50 (1977).

[56] C.T. Chen, Y. Ma, and F. Sette, Physical Review A, **40**, 6737 (1989).

[58] R. Chang, *Chemistry* 5th Ed. McGraw-Hill, Inc. (1994).

[59] T. V. Butkhuzi, A. V. Bureyev, A. N. Georgobiani, N. P. Kekelidze, and T. G. Khulordava, J. Cryst. Growth, **117**, 366 (1992).